

Particle hydrodynamics with accurate gradients: a comparison of different formulations

S. Rosswog^{1,2}

¹ University of Hamburg, Hamburger Sternwarte, Gojenbergsweg 112, 21029, Hamburg, Germany

² The Oskar Klein Centre, Department of Astronomy, AlbaNova, Stockholm University, SE-106 91 Stockholm, Sweden

Draft version

ABSTRACT

We compare here several modern versions of SPH with a particular focus on the impact of gradient accuracy. We examine specifically an approximation to the "linearly exact" gradients (aLE) with standard SPH kernel gradients and with linearly reproducing kernels (RPKs) that fulfill the lowest order consistency relations exactly by construction. Most of the explored SPH formulations use shock dissipation (i.e. artificial viscosity and conductivity) with slope-limited reconstruction and parameters that trigger on both shocks and noise. We also compare with a recent particle hydrodynamics formulation that uses both RPKs and Roe's approximate Riemann solver instead of shock dissipation. Not too surprisingly, we find that the shock tests are rather insensitive to the gradient accuracy, but whenever instabilities are involved the gradient accuracy plays a crucial role. The reproducing kernel gradients perform best, but they are closely followed by the much simpler aLE gradients. The Riemann solver approach has some (minor) advantages in the shock tests, but shows some resistance against instability growth and at low resolution the corresponding Kelvin-Helmholtz simulations show substantially slower instability growth than the best shock dissipation approaches. Based on the battery of benchmark tests performed here, we consider a shock dissipation approach with reproducing kernels (our versions V_3 and V_5) as best, but closely followed by a similar version (V_2) that uses the simpler and computationally cheaper aLE gradients.

Key words: hydrodynamics – methods: numerical – instabilities – shock waves – software: simulations

1 INTRODUCTION

Smooth particle hydrodynamics (SPH) is the "archetypical" mesh-free hydrodynamics method of astrophysical gas dynamics (Lucy 1977; Gingold & Monaghan 1977; Benz 1990; Monaghan 1992). It has a number of benefits that include its natural adaptivity, the ease with which it treats vacuum (without needing an artificial background medium or "atmosphere"), its excellent advection properties and its Galilean invariance. For a broad overview over SPH we refer to a number extensive review articles (Monaghan 2005; Rosswog 2009; Price 2012; Rosswog 2015b; Rosswog 2026). Simulating particle-based gas flows is still a relatively young field compared to Eulerian gas dynamics, and much development is still ongoing, both in terms of improving the methodology and in terms of spreading into new research areas. While having originated from (non-relativistic) astrophysics, SPH has by now found many industrial applications, see e.g. Monaghan (2012) and Quinlan & Tong (2021). On the astrophysics side, the last years have seen much development towards relativistic particle hydrodynamics, either in special relativity (Rosswog 2010a, 2011, 2015a; Kitajima

et al. 2026), in general relativistic hydrodynamics in a fixed metric (Rosswog 2010b; Tejeda et al. 2017; Liptai & Price 2019), or, more recently, in fully dynamical numerical relativity, see Rosswog & Diener (2021); Diener et al. (2022); Rosswog et al. (2023); Magnall et al. (2023) and the dedicated book chapter in Bambi et al. (2025).

One of SPH's pivotal strengths is that it can be formulated in way so that mass, energy, momentum and angular momentum are conserved exactly¹. The straight forward exact conservation is in standard SPH guaranteed by the anti-symmetries of the kernel gradients $\nabla_a W_{ab} = -\nabla_b W_{ab}$ (ensuring exact conservation of energy and momentum) and by kernel gradients pointing exactly along the line connecting two particles $\nabla_a W_{ab} \propto \hat{e}_{ab}$ (ensuring angular momentum conservation).

It has been known for some time that gradient estimates that are based on direct gradients of the smoothing kernel are not particularly accurate, see e.g. Abel (2011); Garcia-Senz et al. (2012); Rosswog (2015a); Frontiere et al. (2017), and one may wonder

* E-mail: stephan.rosswog@astro.su.se

¹ This is true if the time integration is exact, in practice time integration and fast, but approximate treatment of forces can lead to small non-conservation effects.

2 Rosswog

whether sacrificing exact angular momentum conservation in favor of more accurate gradients may overall be a better compromise. Many accurate mesh-less gradient prescriptions exist, see Sec. 2.7 in Rosswog (2026), but to our knowledge none of them can guarantee exact angular momentum conservation *and* exactly reproduce the gradients of linear functions. There are several approaches where *exact* angular momentum conservation was sacrificed in favor of good gradient accuracy (Garcia-Senz et al. 2012; Frontiere et al. 2017; Rosswog 2025; Sandnes et al. 2025) and all these studies found favorable results for the more accurate gradients. Where it has been quantified, see for example Frontiere et al. (2017) or Fig. 30 in Rosswog (2020), the non-conservation has been found to be well below 1%, and -at least in the study of Rosswog (2020) – this small non-conservation is dominated by approximate gravitational forces via a tree-approach rather than the gradient prescription.

In this paper we are particularly interested in

- a) the effects of improved gradient accuracy in standard hydrodynamic benchmark tests,
- b) a comparison between simple gradient correction methods that only need the inversion of a 3×3 matrix (Sec. 2.2.1) with the reproducing kernel (RPK) method that ensures an exact partition of unity/nullity (Sec. 2.2.2), but is also computationally more expensive and
- c) how well a shock dissipation approach with RPKs performs in comparison to a recently suggested RPK method (Rosswog 2025) that uses Roe's approximate Riemann solver (Roe 1986).

This paper is structured as follows. In Sec. 2.1 we concisely summarize the basic SPH approximation, the conditions that need to be fulfilled for high accuracy and we discuss several approaches to approximate gradients at the particle positions. Apart from standard SPH kernel gradients, we discuss an approximation to "linearly exact gradients" that has to our knowledge not been used in astrophysics and we summarize the construction of RPKs and of their gradients. In Sec. 2.3 we summarize our "shock dissipation", i.e. artificial viscosity and conductivity, terms. Here we enhance a Cullen & Dehnen (2010) type shock trigger with a sensitive trigger on noise that is based Rosswog (2015a). We then formulate in Sec. 2.4 five different SPH versions the abilities of which are explored in the tests described in Sec. 3. In this section we explore shocks, instabilities and complex Riemann problems due to Schulz-Rinne. We finally summarize our findings in Sec. 4.

2 METHODOLOGY

2.1 SPH approximation

The standard SPH way of smoothly approximating a function f that is known at particle positions b is

$$\tilde{f}(\vec{r}) = \sum_b V_b f_b W_h(\vec{r} - \vec{r}_b) \equiv \sum_b f_b \Phi_b^h(\vec{r}), \quad (1)$$

where for the particle volume V_b one usually uses $\frac{m_b}{\rho_b}$, W_h is the SPH smoothing kernel whose support size is determined by the smoothing length h , which can be considered as a function of position, i.e. $h = h(\vec{r})$. We have further introduced the shape function $\Phi_b^h(\vec{r}) = V_b W_h(\vec{r} - \vec{r}_b)$. To quantitatively understand the accuracy of this approximation, insert a Taylor expansion of f_b around \vec{r}_a

$$f_b = f_a + (\partial_i f)_a (\vec{r}_{ba})^i + \frac{1}{2!} (\partial_{jk} f)_a (\vec{r}_{ba})^j (\vec{r}_{ba})^k + \dots \quad (2)$$

with $\vec{r}_{ba} = \vec{r}_b - \vec{r}_a$ into Eq. (1) and compare the resulting expression with Eq. (1), evaluated at $\vec{r} = \vec{r}_a$. Requiring that $\tilde{f}(\vec{r}_a)$ is a good approximation to f_a immediately provides the following conditions on the discrete moments

$$(M_0)_a = \sum_b \Phi_b^h(\vec{r}_a) \stackrel{!}{=} 1 \quad (3)$$

$$(M_1^i)_a = \sum_b \vec{r}_{ba}^i \Phi_b^h(\vec{r}_a) \stackrel{!}{=} 0 \quad (4)$$

$$(M_2^{jk})_a = \sum_b \vec{r}_{ba}^j \vec{r}_{ba}^k \Phi_b^h(\vec{r}_a) \stackrel{!}{=} 0 \quad (5)$$

...

for an accurate approximation. So to reproduce a constant function exactly, the condition (3) needs to be fulfilled, to reproduce a linear function exactly condition (4) needs to be fulfilled and so on. The condition on M_0 is of course just the requirement of an exact "partition of unity" and for later use we write it explicitly, together with its gradient, as

$$\sum_b V_b W_h(r_{ab}) = 1 \quad \text{and} \quad \sum_b V_b \nabla W_h(r_{ab}) = 0. \quad (6)$$

The latter condition is sometimes referred to as "partition of nullity". In standard SPH these "zero order consistency relations" are not enforced and only approximately fulfilled.

2.2 Gradients in SPH

The conventional way to calculate SPH gradients is to straight forwardly apply the nabla operator to expression Eq. (1)

$$\nabla f(\vec{r}) = \sum_b V_b f_b \nabla W_h(\vec{r} - \vec{r}_b), \quad (7)$$

or, when specifying to the gradient at the position of a particle a , \vec{r}_a ,

$$(\nabla f)_a = \sum_b V_b f_b \nabla W_{h_a}(\vec{r}_a - \vec{r}_b). \quad (8)$$

For the radial kernels that are usually used in SPH, $W_h(\vec{r}_a - \vec{r}_b) = W_h(|\vec{r}_a - \vec{r}_b|)$, this has the virtue of anti-symmetry,

$$\nabla_a W_h(|\vec{r}_a - \vec{r}_b|) = -\nabla_b W_h(|\vec{r}_a - \vec{r}_b|), \quad (9)$$

which allows in a straight-forward way to ensure the conservation of momentum and energy in SPH. Moreover, since the kernel gradient points along the line connecting particles a and b ,

$$\nabla_a W_h(|\vec{r} - \vec{r}_b|) \propto \vec{r}_a - \vec{r}_b \quad (10)$$

angular momentum can be easily conserved by construction, see e.g. Sec. 2.3 in Rosswog (2026) for a recent review.

This straight forward enforcement of exact conservation is a very good reason to use the above gradient prescription, but it comes at the price of only approximately fulfilling the lowest order interpolation consistency relations and such gradients are not very accurate, see below. How well the consistency conditions are fulfilled in practice depends usually on the local particle distribution, which in turn depends on the combination of kernel function and contributing neighbors. While the consistency relations can be fulfilled to good accuracy e.g. by the combination of Wendland kernels (Wendland 1995) with many neighbor particles (i.e. a large smoothing length), this comes at the price of long neighbor lists which require a non-negligible computational burden. As we will show below, see Fig. 1, even a seemingly small deviation from a regular particle distribution can lead to a serious loss of gradient

accuracy.

There are, however, many ways to calculate accurate gradients at particle positions, see Sec. 2.7 in Rosswog (2026) for an overview, though the gained gradient accuracy usually comes at the price of sacrificing property Eq. (10) and thus losing exact angular momentum conservation. Here we want to explore in particular an approximation to the linearly exact (LE) gradients, see Sec. 2.2.1 and "reproducing kernel gradients" (Liu et al. 1995), which are derived by explicitly enforcing the consistency relations up to linear order, see Sec. 2.2.2.

2.2.1 Linearly exact gradients and their approximations

Linearly exact (LE) gradients can be obtained (Price 2004) by inserting Eq. (2) into the RHS of Eq. (8)

$$\sum_b V_b f_b \nabla_a W_h(r_{ab}) = \sum_b V_b \{f_a + (\nabla f)_a \cdot (\vec{r}_b - \vec{r}_a) + \dots\} \nabla_a W_h(r_{ab}). \quad (11)$$

Rearranging and solving for the gradient yields

$$(\nabla^i f)_a^{\text{LE}} = C_a^{ik} \sum_b V_b (f_b - f_a) \nabla_a^k W_h(r_{ab}) = \sum_b V_b f_{ba} \widetilde{\nabla_a^k W_h}(r_{ab}), \quad (12)$$

where $f_{ba} = f_b - f_a$, the "corrected kernel gradient" reads

$$\widetilde{\nabla_a^k W_h}(r_{ab}) = C_a^{ik} \nabla_a^k W_h(r_{ab}) \quad (13)$$

and the correction matrix is given by

$$C_a^{ik} = \left(\sum_b V_b (\vec{r}_b - \vec{r}_a)^i \nabla_a^k W_h(r_{ab}) \right)^{-1}. \quad (14)$$

If we assume that we have to a good accuracy a partition of unity, see the second relation in Eq. (6), we can neglect the term containing f_a in Eq. (12) and approximate the gradient as

$$(\nabla^i f)_a^{\text{aLE}} = C_a^{ik} \sum_b V_b f_b \nabla_a^k W_h(r_{ab}). \quad (15)$$

The comparison of Eq. (15) with Eq. (8) proposes

$$\nabla_a^i W_h(r_{ab}) \rightarrow C_a^{ik} \nabla_a^k W_h(r_{ab}) \text{ and } \nabla_b^i W_h(r_{ba}) \rightarrow C_b^{ik} \nabla_b^k W_h(r_{ba}), \quad (16)$$

where the second relation, which is needed below, results simply from exchanging $a \leftrightarrow b$.

As pointed out in Rosswog (2015a), Eq. (12) is equivalent to an approach that was derived by discretizing an integral (Garcia-Senz et al. 2012; Cabezon et al. 2012). Their resulting "integral approximation" (IA) gradient prescription reads

$$(\nabla^i f)_a^{\text{IA}} = D_a^{ik} \sum_b V_b (f_b - f_a) \vec{r}_{ba}^k W_h(r_{ab}), \quad (17)$$

$$\approx D_a^{ik} \sum_b V_b f_b \vec{r}_{ba}^k W_h(r_{ab}), \quad (18)$$

where their correction matrix is

$$D_a^{ik} = \left(\sum_b V_b (\vec{r}_a - \vec{r}_b)^i (\vec{r}_a - \vec{r}_b)^k W_h(r_{ab}) \right)^{-1} \quad (19)$$

and when neglecting the f_a -term in Eq. (18) we have assumed that Eq. (4) is fulfilled. To see that this approach is equivalent to Eq. (12), start from

$$\nabla_a W_h(r_{ab}) = \frac{\partial}{\partial \vec{r}_a} W \left(\frac{|\vec{r}_a - \vec{r}_b|}{h_a} \right) = \frac{\partial W}{\partial u} \frac{\partial u}{\partial \vec{r}_a} = \frac{\partial W}{\partial u} \frac{\vec{r}_a - \vec{r}_b}{h_a |\vec{r}_a - \vec{r}_b|}, \quad (20)$$

where $u \equiv |\vec{r}_a - \vec{r}_b|/h_a$. Since $\partial W/\partial u < 0$, we can write this as

$$\nabla_a W_h(r_{ab}) = -\frac{\partial W}{\partial u} \frac{\vec{r}_b - \vec{r}_a}{h_a |\vec{r}_a - \vec{r}_b|} \equiv (\vec{r}_b - \vec{r}_a) \tilde{W}_{h_a}(\vec{r}_{ab}), \quad (21)$$

where \tilde{W} is another valid, positive definitive kernel with finite support. Inserting Eq. (21) into the LE-gradient Eq. (12) we find

$$(\nabla_a^i f)^{\text{IA}} = \left(\sum_l V_l (\vec{r}_b - \vec{r}_a)^i (\vec{r}_b - \vec{r}_a)^k \tilde{W}_{h_a}(\vec{r}_{ab}) \right)^{-1} \left\{ \sum_b V_b (f_b - f_a) (\vec{r}_b - \vec{r}_a)^k \tilde{W}_{h_a}(\vec{r}_{ab}) \right\}, \quad (22)$$

which is, apart from using \tilde{W} instead of W , the gradient expression found by discretizing an integral expression.

Calculating such correction matrix gradients comes at a very small computational price, since only a 3×3 matrix, either Eq. (14) or Eq. (19), needs to be inverted and this can be done analytically.

2.2.2 Reproducing kernel gradients

The standard SPH-approximation neither exactly reproduces constant nor linear functions. This, however, can be enforced (Liu et al. 1995), by enhancing the kernel functions with additional parameters A and B^i ,

$$\mathcal{W}_{ab}(\vec{r}_{ab}) \equiv A_a \left[1 + B_a^i (\vec{r}_{ab})^i \right] \tilde{W}_{ab}, \quad (23)$$

where \tilde{W}_{ab} is a symmetrized kernel function, e.g.

$$\bar{W}_{ab} = \frac{1}{2} [W_{h_a}(r_{ab}) + W_{h_b}(r_{ab})]. \quad (24)$$

The parameters A and B^i are determined at every point (here labelled a) so that \mathcal{W} exactly reproduces the discrete first-order consistency relations

$$\sum_b V_b \mathcal{W}_{ab} = 1 \quad \text{and} \quad \sum_b (\vec{r}_{ab})^i V_b \mathcal{W}_{ab} = 0, \quad (25)$$

see the moment conditions Eqs. (3) and (4). The price for this exact reproduction is that the kernel is, apart from the computational effort to determine A and B^i , no longer guaranteed to be radial due to the B^i -term. This property is in standard SPH responsible for exact angular momentum conservation. It is, however, possible to relatively straight-forwardly write a set of equations that conserves energy, momentum and mass, if density summation is used, but not necessarily angular momentum, since the mutual accelerations can no longer be guaranteed to be along the line connecting two particles, see Sect. 2.3 in Rosswog (2026).

Once the kernels are explicitly constructed, see Appendix A for the details, one can approximate a function f and its derivative via

$$f(\vec{r}_a) = \sum_b V_b f_b \mathcal{W}_{ab} \quad \text{and} \quad \nabla^k f_a = \sum_b V_b f_b \partial_k \mathcal{W}_{ab}. \quad (26)$$

These expressions look very similar to standard SPH approximations, but they *exactly* reproduce linear functions on a discrete level, which the SPH equations do not. The gradient of \bar{W}_{ab} can be written as

$$\nabla_a \bar{W}_{ab} = \frac{\nabla_a W_h(r_{ab}) + \nabla_b W_h(r_{ab})}{2} = \frac{\nabla_a W_h(r_{ab}) - \nabla_b W_h(r_{ab})}{2}, \quad (27)$$

which suggests the replacement

$$\nabla_a \bar{W}_{ab} \rightarrow (\nabla \mathcal{W})_{ab} \equiv \frac{1}{2} [\nabla_a \mathcal{W}_{ab} - \nabla_b \mathcal{W}_{ba}]. \quad (28)$$

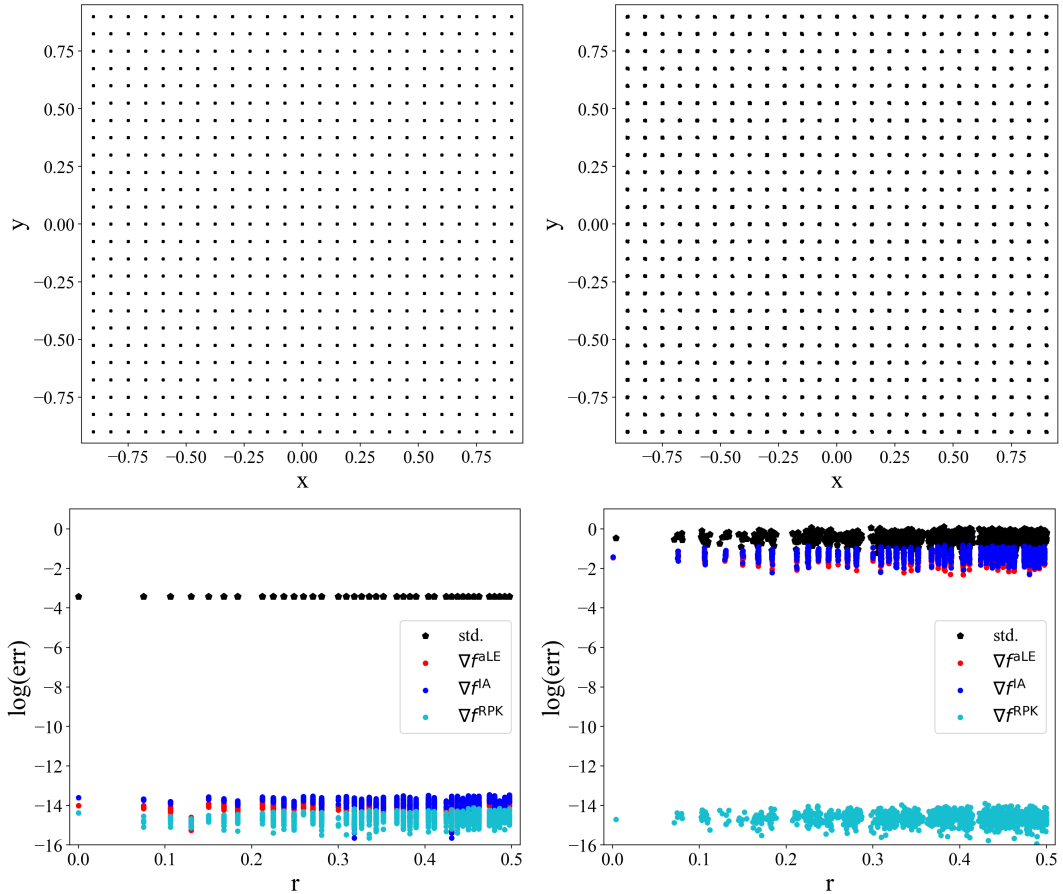


Figure 1. Numerical experiment to measure gradient accuracy. The upper row shows the particle positions, exactly arranged on a cubic lattice (left), and the same lattice, but with each particle coordinate shifted by a small random number chosen uniformly from the interval [-0.001,0.001]. The second row shows the gradient errors for both particle configurations for the different gradient gradient prescription. Note that the hardly visible randomization of the positions leads to a serious gradient deterioration for the standard, the aLE- and the IA-gradient. Please see the main text for the exact definitions of the gradient estimates.

Various particle hydrodynamics schemes based on reproducing kernels have been developed in recent times, for example the artificial viscosity-based codes CRKSPH (Frontiere et al. 2017) and REMIX (Sandnes et al. 2025) or a Riemann solver-based approach with reproducing kernels which is described in Rosswog (2025).

2.2.3 Measuring gradient accuracy

We show in Fig. 1 an experiment to scrutinize the gradient approximations. In a first step, we use particles that are exactly arranged on a cubic lattice and, in a second step, this lattice is randomly disturbed by a small amplitude, see the upper two panels of Fig. 1. In the randomized case, right column Fig. 1, each particle coordinate was displaced by a random number chosen uniformly from the interval [-0.001,0.001]. Each particle is assigned a function $\mathbf{f}(\vec{r}) = (-x, 0, 0)$ and we measure the error between the numerically determined gradient and the exact result, $\varepsilon \equiv |\nabla f^{\text{num}} - \nabla f^{\text{ex}}| / |\nabla f^{\text{ex}}|$. Note that the hardly visible perturbation (right panel in Fig. 1) has a serious impact on the accuracy of the standard and the IA- and aLE-gradients, see Eqs. (8), (15) and (18), while the RPK gradient estimate reproduces the theoretical result to within machine precision whether the particle distribution is randomized or not. The IA- and the aLE-gradients perform very similar in this experiment,

with a small advantage for aLE-gradients. This small difference, however, may not be relevant in practical dynamical benchmarks. Also note that both correction matrix approaches assumed in their derivation that a partition of unity is fulfilled to a good approximation. Since we see here that even small deviations from a regular particle distribution lead to a strong loss of accuracy and it is difficult to predict how (ir)regular the particle distribution will become in a dynamical simulation, one may wonder whether such matrix correction approaches are actually useful in practice. As will be shown below, however, they turn out to deliver clearly better results than the standard SPH gradients.

2.3 Shock dissipation

Before we come to the explicit SPH formulations we want to summarize how we treat shocks. The most common approach to handle shocks in SPH is via "artificial dissipation" in the form of "artificial viscosity" (acting on the momentum equation), often enhanced by "artificial conductivity" (acting on the energy equation). We will collectively refer to them as "shock dissipation". The main purposes of shock dissipation are i) to prevent a steepening sound wave from becoming too steep to be treated numerically, ii) to produce the correct entropy in a shock and iii) to ensure the Rankine-Hugoniot shock jump conditions, see Mattsson & Rider (2015) for

a wider historical perspective on shock dissipation. Note that the comparison with Riemann solvers also suggests to use dissipative terms for the continuity equation so that particles can exchange mass in a conservative way. This has so far been applied only in a few cases, but there the authors find good results (Read & Hayfield 2012; Sandnes et al. 2025).

The major change when implementing artificial viscosity is to enhance the physical pressure P by an artificial pressure Q ,

$$P \rightarrow \tilde{P} = P + Q, \quad (29)$$

wherever it occurs. We use (Monaghan & Gingold 1983)

$$Q_a = \rho_a \left(-\alpha c_{s,a} \mu_a + \beta \mu_a^2 \right), \quad (30)$$

where the velocity jump estimate is

$$\mu_a = \min \left(0, \frac{(\vec{v}_{ab} \cdot \vec{r}_{ab}) h_a}{r_{ab}^2 + \epsilon^2 h_a^2} \right). \quad (31)$$

Here, $\vec{v}_{ab} = \vec{v}_a - \vec{v}_b$, $\vec{r}_{ab} = \vec{r}_a - \vec{r}_b$, $r_{ab}^2 = \vec{r}_{ab} \cdot \vec{r}_{ab}$ and α, β and ϵ are numerical parameters with typical values 1, 2 and 0.1 and c_s is the sound speed. The ϵ -term in the denominator avoids divergence and the min-function switches off the artificial pressure for receding particles ($\vec{v}_{ab} \cdot \vec{r}_{ab} > 0$). Applying dissipation only in converging flows is a noteworthy difference between shock dissipation and standard Riemann solver approaches where the dissipation acts in both compressing and expanding flows.

We also add a small amount of artificial conductivity (Price 2008) to energy equation

$$\left(\frac{du}{dt} \right)_{a,AC} = \alpha_u \sum_b \frac{m_b}{\bar{\rho}_{ab}} \sqrt{\frac{|P_a - P_b|}{\bar{\rho}_{ab}}} (u_a - u_b) \hat{e}_{ab} \cdot \nabla W_h(r_{ab}), \quad (32)$$

with $\alpha_u = 0.05$ which has been found advantageous in shocks and instabilities (Rosswog & Price 2007; Price 2008; Valdarnini 2012).

2.3.1 Controlling dissipation

The straight forward implementation of shock dissipation may lead to unwanted dissipation where it is not needed, we therefore perform i) a slope-limited linear reconstruction in the dissipative terms as in the MAGMA2 code (Rosswog 2020) and ii) we steer the dissipation parameters α and $\beta = 2\alpha$.

For the slope limited reconstruction, we replace the velocity values at the particle positions in the \vec{v}_{ab} term in Eq. (31), by values reconstructed to the mid-point between the particles both from a - and the b -side

$$v_a^{i,\text{rec}} = v_a^i - \frac{1}{2} \Psi(\nabla v_a^i, \nabla v_b^i) \cdot \vec{r}_{ab} \quad v_b^{i,\text{rec}} = v_b^i + \frac{1}{2} \Psi(\nabla v_a^i, \nabla v_b^i) \cdot \vec{r}_{ab}. \quad (33)$$

Similarly, we replace $u_a - u_b$ in Eq. (32) by u -values that are reconstructed from both sides similar to Eq. (33). The quantity Ψ is a slope limiter for which we use the vanAlbada limiter (van Albada et al. 1982)

$$\Psi_{\text{VA}}(x, y) = \begin{cases} \frac{(x^2 + \epsilon^2)y + (y^2 + \epsilon^2)x}{x^2 + y^2 + 2\epsilon^2} & \text{if } xy > 0, \\ 0 & \text{otherwise.} \end{cases} \quad (34)$$

The limiter is insensitive to the exact value of ϵ , here, we use $\epsilon^2 = 10^{-6}$. In Rosswog (2025) we had compared various slope limiters and found particularly good results for the vanAlbada limiter. Such slope-limited reconstruction approaches in shock dissipation terms have turned out to be very efficient in suppressing unwanted dissipation (Christensen 1990; Frontiere et al. 2017;

Rosswog 2020; Rosswog & Diener 2021; Sandnes et al. 2025). To reduce dissipation even further, the dissipation parameter α can in addition be made time-dependent as originally suggested by Morris & Monaghan (1997), so that it rises quickly where needed and decays exponentially otherwise. If no higher dissipation parameter value is triggered, see below, α evolves according to

$$\frac{d\alpha_a}{dt} = -\frac{\alpha_a(t) - \alpha_{\min}}{\tau_a}, \quad (35)$$

where α_{\min} represents a minimum, “floor” value for the viscosity parameter and τ_a is an individual decay time scale at particle a . Here we use $\alpha_{\min} = 0$ and $\tau_a = 30h_a/c_{s,a}$. If instead a higher dissipation parameter $\alpha_{a,\text{des}}$ is needed, $\alpha_a(t)$ is instantaneously replaced with $\alpha_{a,\text{des}}$. Cullen & Dehnen (2010) suggested as shock-triggered dissipation parameter

$$\alpha_{a,\text{shock}} = \alpha_{\max} \frac{T_a^s}{T_a^s + c_a^2/h_a^2}, \quad (36)$$

where the shock trigger²,

$$T_a^s = \max \left[-\frac{d(\nabla \cdot \vec{v})_a}{dt}, 0 \right], \quad (37)$$

measures a temporarily increasing compression. We found that this trigger works well in shocks, but it triggers too little dissipation in the challenging Schulz-Rinne tests, see Fig. C1 in the Appendix. We therefore add an additional trigger on noise that measures the strength of local sign fluctuations in $\nabla \cdot \vec{v}$ (Rosswog 2015a). To this end we calculate average $\nabla \cdot \vec{v}$ values separately for positive and negative signs:

$$\mathcal{S}_a^+ = \frac{1}{N^+} \sum_{b, \nabla \cdot \vec{v}_b > 0}^{N^+} \nabla \cdot \vec{v}_b \quad \text{and} \quad \mathcal{S}_a^- = -\frac{1}{N^-} \sum_{b, \nabla \cdot \vec{v}_b < 0}^{N^-} \nabla \cdot \vec{v}_b \quad (38)$$

where N^+/N^- are the correspondingly contributing particle numbers in the neighborhood of particle a . The noise trigger then reads

$$T_a^n = \sqrt{\mathcal{S}_a^+ \mathcal{S}_a^-} \quad (39)$$

and it is translated to an α -value via

$$\alpha_{a,\text{noise}} = \alpha_{\max} \frac{T_a^n}{T_a^n + 0.01c_a/h_a}. \quad (40)$$

The final desired dissipation parameter value is then

$$\alpha_a^{\text{des}} = \max(\alpha_{a,\text{shock}}, \alpha_{a,\text{noise}}) \quad (41)$$

and if it exceeds $\alpha_a(t)$ the latter is immediately replaced by α_a^{des} . If there are sign fluctuations, but they are small compared to the reference value in the denominator of Eq. (40), the product is very small. If instead we have uniform expansion or compression in the neighborhood of particle a , either \mathcal{S}_a^+ or \mathcal{S}_a^- will be zero. So only for sign changes and significantly large compressions/expansions will the T^n have a substantial value. Note that we have chosen a small reference value ($0.01c_a/h_a$) in Eq. (40), which we found to work well in detecting noise in Schulz-Rinne tests without triggering too much dissipation in rather smooth flows such as Rayleigh-Taylor or Kelvin-Helmholtz instabilities, see Fig. C2 in the Appendix. Note that although we had chosen $\alpha_{\min} = 0$ in Eq. (35) our sensitive noise triggers causes in the smooth parts of the flow a small base level of $\alpha \approx 0.03$, see Fig. C2.

² They multiplied T_a^s with an additional limiter which we omit here for simplicity.

2.4 SPH formulations

A large variety of SPH formulations can be found by realizing (Price 2004) that the continuity equation can be written as

$$\frac{d\rho}{dt} = \Psi \left[\vec{v} \cdot \nabla \left(\frac{\rho}{\Psi} \right) - \nabla \cdot \left(\frac{\rho \vec{v}}{\Psi} \right) \right], \quad (42)$$

where Ψ is an arbitrary scalar function defined on the particle field, which can, by straight forwardly applying Eq. (8), be translated into

$$\frac{d\rho_a}{dt} = \sum_b m_b \frac{\Psi_a}{\Psi_b} \vec{v}_{ab} \cdot \nabla_a W_h(r_{ab}). \quad (43)$$

The consistent momentum equation is given by

$$\frac{d\vec{v}_a}{dt} = - \sum_b m_b \left(\frac{P_a}{\rho_a^2} \frac{\Psi_a}{\Psi_b} + \frac{P_b}{\rho_b^2} \frac{\Psi_b}{\Psi_a} \right) \nabla_a W_h(r_{ab}) \quad (44)$$

and the corresponding equations for the specific internal energy and the thermokinetic energy $\tilde{e} = u + \vec{v}^2/2$ read

$$\frac{du_a}{dt} = \frac{P_a}{\rho_a^2} \sum_b m_b \frac{\Psi_a}{\Psi_b} \vec{v}_{ab} \cdot \nabla_a W_h(r_{ab}) \quad (45)$$

and

$$\frac{d\tilde{e}_a}{dt} = - \sum_b \left(\frac{\Psi_a}{\Psi_b} \frac{P_a \vec{v}_b}{\rho_a^2} + \frac{\Psi_b}{\Psi_a} \frac{P_b \vec{v}_a}{\rho_b^2} \right) \nabla_a W_h(r_{ab}), \quad (46)$$

respectively.

2.4.1 Version 0 (V_0): "traditional SPH" with cubic spline kernels and constant dissipation

This version serves as a minimum base level: it uses a "vanilla ice" SPH formulation (corresponding to $\Psi = 1$ in the above equations) with a traditional cubic spline kernel with 50 neighbor particles, standard kernel gradients and it applies artificial viscosity with constant parameters $\alpha = \beta/2 = 1$. Explicitly, it reads

$$\rho_a = \sum_b m_b \bar{W}_{ab} \quad (47)$$

$$\left(\frac{d\vec{v}}{dt} \right)_a = - \sum_b m_b \left(\frac{\tilde{P}_a}{\rho_a^2} + \frac{\tilde{P}_b}{\rho_b^2} \right) \nabla_a \bar{W}_{ab} \quad (48)$$

$$\left(\frac{du}{dt} \right)_a = \frac{P_a}{\rho_a^2} \sum_b m_b \vec{v}_{ab} \cdot \nabla_a \bar{W}_{ab}, \quad (49)$$

where the \tilde{P} s denote pressures that are enhanced by an artificial pressure as discussed in Sec. 2.3. Note that we use here always the kernel \bar{W}_{ab} , Eq. (24), and its gradient. This is because it is used in the most involved SPH versions (V_3, V_4, V_5) using reproducing kernels and since a major focus here is on the impact of the gradient accuracy we want to keep the density calculation the same in all versions. It has to be stressed that V_0 is really a combination of non-optimal options and most modern SPH codes use better choices.

2.4.2 Version 1 (V_1): $\Psi = \rho$ with standard kernel gradients

V_1 uses the equation set resulting from $\Psi = \rho$. It has been shown in previous work (Oger et al. 2007; Read et al. 2010; Wadsley et al. 2017; Rosswog 2020) that this version is more accurate when strong gradients are involved. We show a concise comparison for common choices of Ψ in Appendix B which clearly favors $\Psi = \rho$. V_1 further uses standard SPH kernels, but with the Wendland C4

kernel a much better kernel function than V_0 . It applies shock dissipation as described in Sec. 2.3, including slope limited reconstruction (using reproducing kernels in the dissipative terms only) and a steering of the dissipation parameters $\alpha(t)$ and $\beta(t) = 2\alpha(t)$ by means of shock and noise triggers, see Eqs. (36) and (40) and we also apply a small amount of thermal conductivity, see Eq. (32) and in the "jump terms" of this equation we also use reconstructed quantities.

In V_1 the density is calculated via Eq. (47) and the momentum and energy equation read

$$\left(\frac{d\vec{v}}{dt} \right)_a = - \sum_b m_b \left(\frac{\tilde{P}_a + \tilde{P}_b}{\rho_a \rho_b} \right) \nabla_a \bar{W}_{ab} \quad (50)$$

$$\left(\frac{du}{dt} \right)_a = \sum_b m_b \left(\frac{\tilde{P}_a}{\rho_a \rho_b} \right) \vec{v}_{ab} \cdot \nabla_a \bar{W}_{ab} + \left(\frac{du}{dt} \right)_{a,AC}, \quad (51)$$

where we use reproducing kernels in the conductivity term, as in the dissipative terms of V_2, V_3 and V_5 .

V_0 and V_1 are both fully conservative SPH versions, but once with bad and once with good choices.

2.4.3 Version 2 (V_2): $\Psi = \rho$ with aLE-gradients

The only difference between V_1 and V_2 is that we now use aLE-gradients, Eq. (15), instead of the straight forward kernel gradients. We need a replacement of $\nabla_a \bar{W}_{ab}$, Eq. (27) and using Eqs. (15) and (16) yields

$$2\nabla_a^i \bar{W}_{ab} = \nabla_a^i W_{h_a}(r_{ab}) - \nabla_b^i W_{h_b}(r_{ba}) \quad (52)$$

$$\rightarrow C_a^{ik} \nabla_a^k W_{h_a}(r_{ab}) - C_b^{ik} \nabla_b^k W_{h_b}(r_{ba}) \quad (53)$$

so that the replacement becomes

$$\nabla_a^i \bar{W}_{ab} \rightarrow \left(\widetilde{\nabla W} \right)_{ab}^i \equiv \frac{C_a^{ik} \nabla_a^k W_{h_a}(r_{ab}) + C_b^{ik} \nabla_b^k W_{h_b}(r_{ab})}{2}, \quad (54)$$

where we have used $\nabla_b^k W_{h_b}(r_{ab}) = -\nabla_a^k W_{h_b}(r_{ab})$. In V_2 the density is again calculated via Eq. (47) and the momentum and energy equations read

$$\left(\frac{d\vec{v}}{dt} \right)_a = - \sum_b m_b \left(\frac{\tilde{P}_a + \tilde{P}_b}{\rho_a \rho_b} \right) \left(\widetilde{\nabla W} \right)_{ab} \quad (55)$$

$$\left(\frac{du}{dt} \right)_a = \sum_b m_b \left(\frac{\tilde{P}_a}{\rho_a \rho_b} \right) \vec{v}_{ab} \cdot \left(\widetilde{\nabla W} \right)_{ab} + \left(\frac{du}{dt} \right)_{a,AC}. \quad (56)$$

2.4.4 Version 3 (V_3): $\Psi = \rho$ with reproducing kernel gradients

V_3 goes one step further and uses the reproducing kernel gradients, Eq. (28) instead of the aLE-gradients. In V_3 the density is calculated via Eq. (47) and the momentum and energy equations read

$$\left(\frac{d\vec{v}}{dt} \right)_a = - \sum_b m_b \left(\frac{\tilde{P}_a + \tilde{P}_b}{\rho_a \rho_b} \right) (\nabla \mathcal{W})_{ab} \quad (57)$$

$$\left(\frac{du}{dt} \right)_a = \sum_b m_b \left(\frac{\tilde{P}_a}{\rho_a \rho_b} \right) \vec{v}_{ab} \cdot (\nabla \mathcal{W})_{ab} + \left(\frac{du}{dt} \right)_{a,AC}. \quad (58)$$

2.4.5 Version 4 (V_4): reproducing kernels and approximate Riemann solver

The V_4 equation set was suggested in Rosswog (2025), it makes use of reproducing kernels and uses Roe's approximate Riemann solver

(Roe 1986). The starting point is a common set of Smoothed Particle Hydrodynamics (SPH) equations (Parshikov & Medin 2002; Liu & Liu 2003)

$$\rho_a = \sum_b m_b \bar{W}_{ab} \quad (59)$$

$$\frac{d\vec{v}_a}{dt} = -\sum_b m_b \frac{P_a + P_b}{\rho_a \rho_b} \nabla_a \bar{W}_{ab} \quad (60)$$

$$\frac{du_a}{dt} = \frac{1}{2} \sum_b m_b \frac{P_a + P_b}{\rho_a \rho_b} \vec{v}_{ab} \cdot \nabla_a \bar{W}_{ab}. \quad (61)$$

The main idea is to solve a one-dimensional Riemann problem at the midpoint between each pair of interacting particles a and b and to replace averages of particle values by the solution of a Riemann problem

$$\frac{P_a + P_b}{2} \rightarrow P_{ab}^* \quad \text{and} \quad \frac{\tilde{v}_a + \tilde{v}_b}{2} \rightarrow v_{ab}^*, \quad (62)$$

where the $*$ labels the contact discontinuity state in a Riemann problem, see e.g. Toro (2009), and the ab -index refers to the solution between state a and b . In V_4 the density is calculated via Eq. (47) and the momentum and energy equations become

$$\frac{d\vec{v}_a}{dt} = -\frac{2}{\rho_a} \sum_b V_b P_{ab}^* (\nabla \mathcal{W})_{ab} \quad (63)$$

$$\frac{du_a}{dt} = \frac{2}{\rho_a} \sum_b V_b P_{ab}^* (\vec{v}_a - \vec{v}_{ab}^*) \cdot (\nabla \mathcal{W})_{ab}. \quad (64)$$

We use Roe's approximate Riemann solver (Roe 1986) for the star state:

$$v_{ab}^* = \frac{1}{2} \left((\vec{v}_a + \vec{v}_b) \cdot \hat{e}_{ab} + \frac{P_b - P_a}{C_{RL}} \right) \quad (65)$$

$$P_{ab}^* = \frac{1}{2} \left(P_a + P_b + C_{RL} \frac{(\vec{v}_b - \vec{v}_a) \cdot \hat{e}_{ab}}{C_{RL}} \right), \quad (66)$$

where the "densitized" Roe-averaged Lagrangian sound speed (the dimension is density times velocity) is

$$C_{RL} = \frac{c_{s,a} \rho_a \sqrt{\rho_a} + c_{s,b} \rho_b \sqrt{\rho_b}}{\sqrt{\rho_a} + \sqrt{\rho_b}} \quad (67)$$

and $c_{s,k}$ is the sound speed of particle k . If, for a moment, we ignore the terms that involve the pressure and velocity differences in Eqs. (65) and (66), we have

$$v_{ab}^* \approx \frac{\vec{v}_a + \vec{v}_b}{2} \cdot \hat{e}_{ab} \quad \text{and} \quad P_{ab}^* \approx \frac{P_a + P_b}{2}. \quad (68)$$

By inserting these expressions into Eqs. (63) and (64) we obviously recover the inviscid equations (60) and (61), therefore *the terms involving the differences in Eqs. (65) and (66) are responsible for the dissipation*. It is in these terms where we apply reconstructed pressures and velocities as explained in Sec. 2.3. So, for perfectly reconstructed smooth flows, where the reconstructed values on both sides of the midpoint are the same, the dissipative terms vanish and one effectively solves the inviscid hydrodynamics equations.

2.4.6 Version 5 (V_5): like V_4 , but with shock dissipation instead of Riemann solver

V_5 solves the Eqs. (59)-(61) with the replacement $\nabla_a \bar{W}_{ab} \rightarrow (\nabla \mathcal{W})_{ab}$, but instead of using an approximate Riemann solver, it uses shock dissipation. In V_5 the momentum and energy equation

read

$$\frac{d\vec{v}_a}{dt} = -\sum_b m_b \frac{\tilde{P}_a + \tilde{P}_b}{\rho_a \rho_b} (\nabla \mathcal{W})_{ab} \quad (69)$$

$$\frac{du_a}{dt} = \frac{1}{2} \sum_b m_b \frac{\tilde{P}_a + \tilde{P}_b}{\rho_a \rho_b} \vec{v}_{ab} \cdot (\nabla \mathcal{W})_{ab} + \left(\frac{du}{dt} \right)_{a,AC}. \quad (70)$$

A comparison between the results obtained with V_4 and V_5 therefore allows to gauge of the effect of shock dissipation vs approximate Roe Riemann solver.

In all of the shown tests we use the Wendland C4 kernel (Wendland 1995)

$$W_{C4}(r) = \sigma (1 - q)_+^6 \left(1 + 6q + \frac{35}{3} q^2 \right), \quad (71)$$

where $q = r/2h$ so that the kernel support extends to $2h$ and the corresponding normalization is $\sigma = \frac{495}{256\pi}$. We use exactly 250 contributing neighbors within the support size $2h_a$ of each particle a . How exactly this is achieved by means of our recursive coordinate bisection tree (Gaston & Rosswog 2011) is described in detail in Rosswog (2020).

3 RESULTS

3.1 Questions to be addressed

In this section we perform a number of common benchmark tests to probe the abilities of the different SPH formulations. In particular, we are interested in the following

- Which quantity should be chosen for the scalar Ψ ?
- Is an additional trigger on noise beneficial in complex shock tests?
- How important is the gradient accuracy for specific tests?
- How much better are the reproducing kernel gradients than the standard kernel gradients and the aLE gradients? The aLE gradients are substantially cheaper to calculate (only a 3×3 matrix needs to be inverted) than the RPK gradients (much more matrix algebra, see Appendix A), and, from a pragmatic point of view, one may wonder whether the aLE-gradients are good enough.
- How does the recently suggested RPK gradient hydrodynamics version that uses Roe's Riemann solver (V_4) compare to the same equation set, but with shock dissipation rather than a Riemann solver? In other words, how different are the results between Riemann solver and shock dissipation?

To keep the parameter space to be explored under control, we address the first two questions in Appendices B and C). We show in Appendix B several tests for common choices of Ψ and find a clear preference for $\Psi = \rho$. This result is consistent with earlier work (Oger et al. 2007; Read et al. 2010; Wadsley et al. 2017; Rosswog 2020). In Appendix C, we compare for a Schulz-Rinne test case dissipation triggered only with the Cullen & Dehnen (2010) shock trigger with a simulation that additionally applies the noise trigger described above. As shown in Figs. C1 and C2, this trigger provides an appropriate amount of dissipation without over-triggering dissipation in smooth flows.

The other questions are addressed in a set of challenging benchmarks, all of which are performed with the 3D code. The first three cases are shock tests (Sects 3.2 to 3.4), followed by two instability tests and, finally, a selection of challenging Schulz-Rinne Riemann problems.

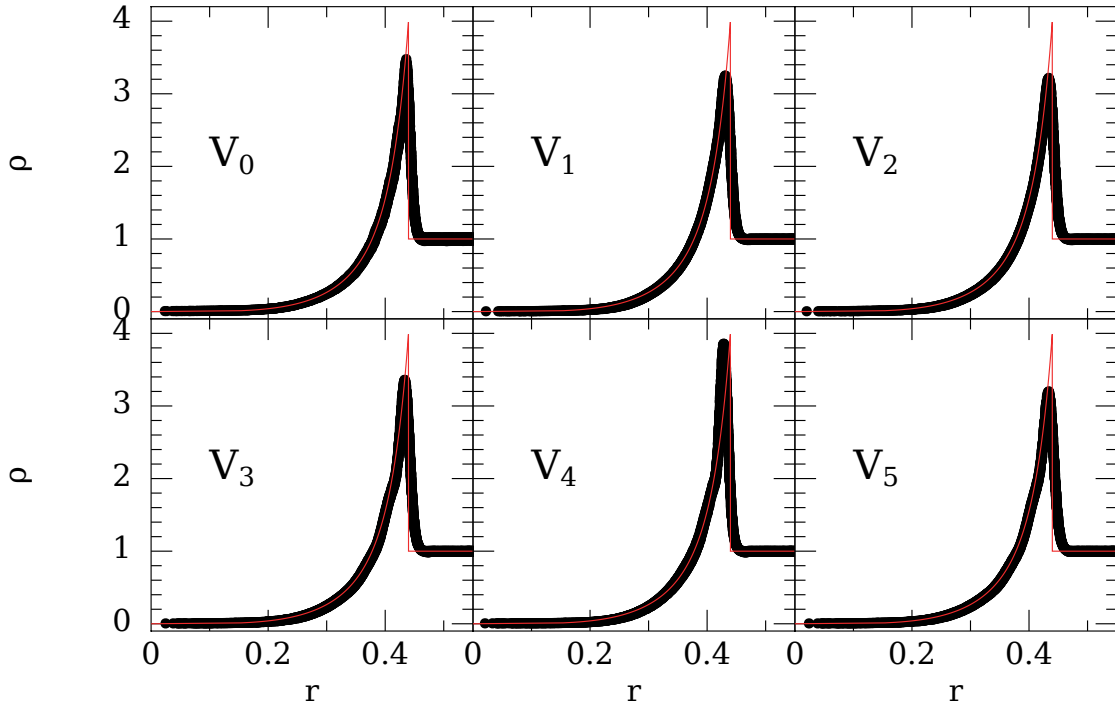


Figure 2. Density in a Sedov explosion at $t = 0.9$ for all SPH versions.

3.2 3D Sedov explosion

The Sedov–Taylor test, a strong initial point-like explosion expanding into a low-density environment, is one of the standard benchmark tests for hydrodynamics codes (Sedov 1959; Taylor 1950). For an explosion energy E and a density of the ambient medium ρ , the blast wave propagates to the radius $r(t) = \beta(Et^2/\rho)^{1/5}$ at time t , where β depends on the adiabatic exponent of the gas (≈ 1.15 in 3D for the $\Gamma = 5/3$ we use). In the strong explosion limit, the density jumps by a factor of $\rho_2/\rho_1 = (\Gamma + 1)/(\Gamma - 1) = 4$ in the shock front, where the numerical value refers to our chosen value of Γ . We place 128^3 particles according to a Centroidal Voronoi Tesselation (Du et al. 1999) in the volume $[-0.5, 0.5]^3$. For an even better particle distribution we perform additional sweeps according to our “Artificial Pressure Method” (APM), see Rosswog (2020) for a detailed description.

Here all the different versions perform pretty well, which is in part due to the careful preparation of the initial particle distribution. From the shock dissipation versions, the reference version V_0 reaches the highest peak, because the chosen cubic spline kernel with only 50 neighbors yields the smallest kernel support size. The Riemann solver version V_4 reaches clearly the highest peak, and in the wake of the shock the RPK gradient versions ($V_3..V_5$) show a small tendency for oscillations. Among the RPK versions V_3 reaches the largest peak height.

3.3 3D spherical Riemann Problem 1

We choose the same parameters as Toro (2009) (apart from a shift of the origin): the computational domain is $[-1, 1]^3$ and the initial conditions are chosen as:

$$(\rho, \vec{v}, P) = \begin{cases} (1.000, 0, 0, 0, 1.0) & \text{for } r < 0.5 \\ (0.125, 0, 0, 0, 0.1) & \text{else.} \end{cases} \quad (72)$$

The solution exhibits a spherical shock wave, a spherical contact surface traveling in the same direction, and a spherical rarefaction wave traveling toward the origin. As initial conditions, we simply placed 200^3 particles on a cubic lattice within $[-1, 1]^3$, together with the surrounding “frozen” particles as the boundary condition. In Fig. 3 we show our particle results in a strip around the x -axis ($|y| < 0.018, |z| < 0.018$) compared with a 400^3 grid cell calculation with the Eulerian weighted average flux method (Toro 2009). Overall, we find very good agreement with the reference solution for all versions $V_1..V_5$. Clearly worst is V_0 which smears out the contact discontinuity region in the density and produces a spurious dip in the velocity. Simply changing to better SPH choices, V_1 , substantially improves the agreement with the reference solution. There is only a very small density overshoot at the beginning of the edge of the rarefaction wave ($x \approx 0.2$), a tiny overshoot of the velocity at the shock front and a very small “pressure blip” at the contact discontinuity. Using the aLE-approximation, V_2 , slightly improves on the pressure blip and essentially shows no velocity overshoot at the shock. V_3 with the RPK gradients improves on the pressure blip, but also shows some velocity overshoot at the shock. V_4 with the RPK Riemann solver approach essentially gets rid of the pressure blip, also shows the velocity overshoot and slightly larger rarefaction wave. This is because the dissipation from the Riemann solver is applied both in expanding and compressing flows, while the shock dissipation of the other versions is only applied in compressing flows, see Eq. (31). Overall, all modern versions perform very well in this test, only the baseline version V_0 shows deficiencies.

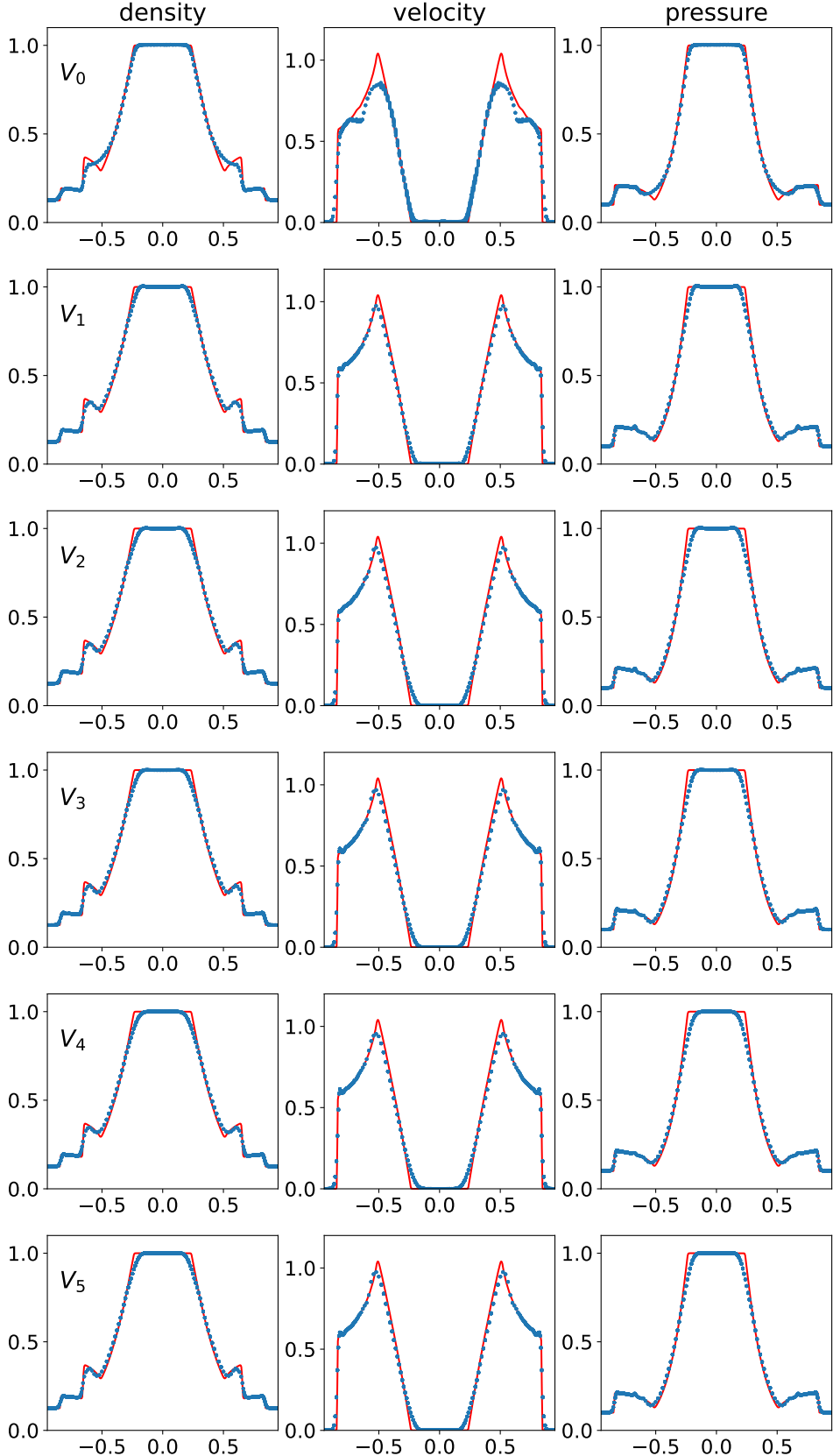


Figure 3. 3D Riemann problem 1 for all SPH versions at $t = 0.2$

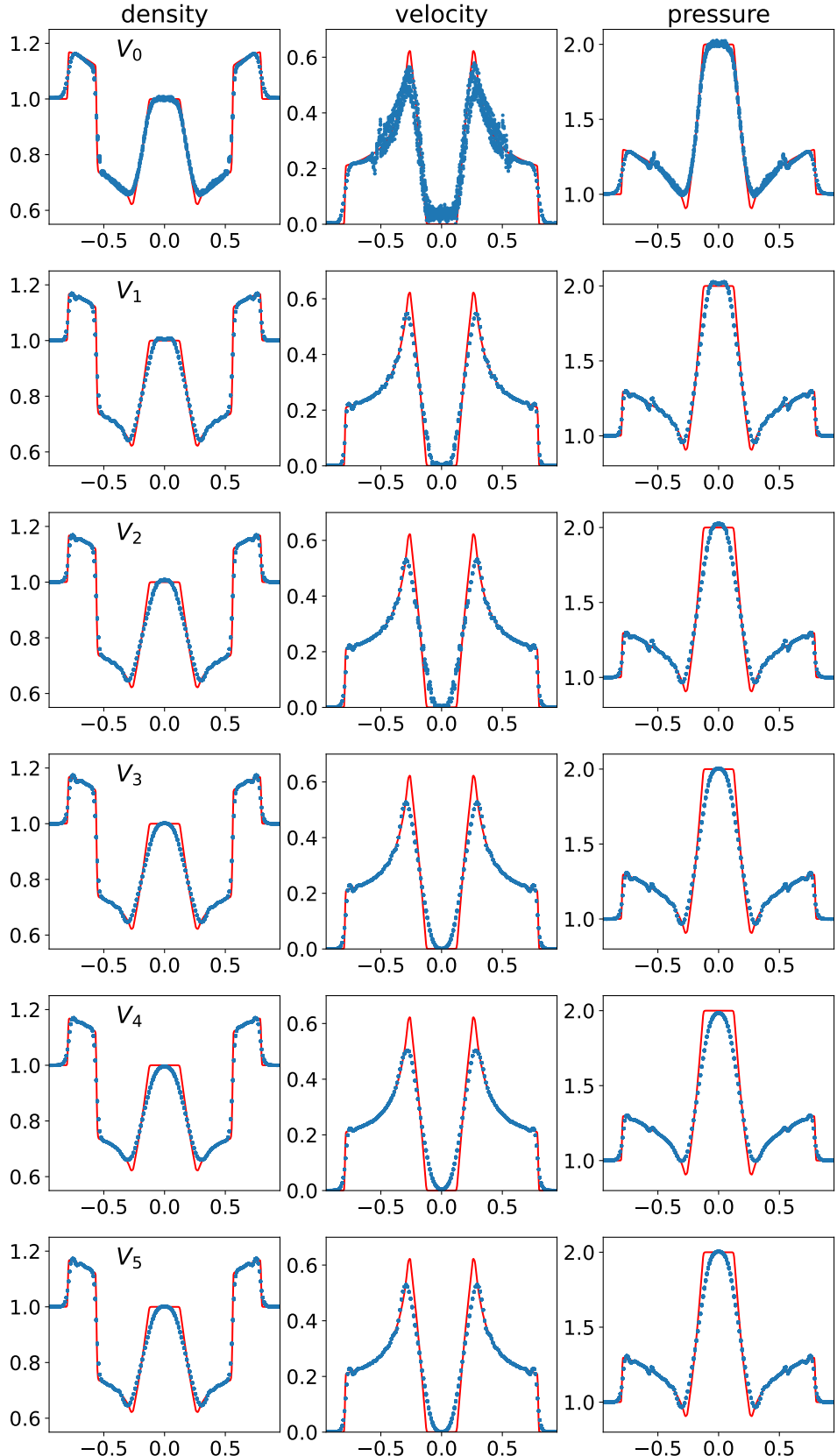


Figure 4. 3D Riemann problem 2 for all SPH versions at $t = 0.2$

3.4 3D spherical Riemann Problem 2

In a second spherical blast wave problem (Toro 2009) we start from

$$(\rho, \vec{v}, P) = \begin{cases} (1.0, 0, 0, 0, 2.0) & \text{for } r < 0.5 \\ (1.0, 0, 0, 0, 1.0) & \text{else} \end{cases} \quad (73)$$

and place again 200^3 particles in the same straightforward way as in the first blast wave problem.

We show in Fig. 4 the results for all five versions. Again, the baseline version V_0 shows substantial artifacts in the velocity. The Riemann solver RPK version V_4 shows the smallest oscillations in the solution, but it is more dissipative at the beginning of the rarefaction wave, again because it applies dissipation to both converging and expanding flows. Here we do see a difference of the gradient accuracy: both the standard SPH gradient (V_1) and the improved aLE-gradient (V_2) show more velocity noise in the inner regions than the RPK gradient versions $V_3..V_5$.

3.5 Kelvin-Helmholtz

Traditional versions of SPH have been shown to struggle with weakly triggered Kelvin-Helmholtz (KH) instabilities (Agertz et al. 2007; McNally et al. 2012), although many recent studies with more sophisticated numerical methods yielded very good results (Frontiere et al. 2017; Rosswog 2020; Sandnes et al. 2025). We focus here on a test setup in which traditional SPH has been shown to fail, even at a rather high resolution in 2D, see McNally et al. (2012). We follow the latter paper (similar setups were used in Frontiere et al. (2017), Rosswog (2020) and Sandnes et al. (2025)), but we use the full 3D code and set up the "2D" test as a thin 3D slice with $N \times N \times 20$ particles (referred to as " N^2 "). For simplicity, the particles are initially placed on a cubic lattice. Periodic boundary conditions are enforced by placing appropriate particle copies outside of the "core" volume. The test is initialized as:

$$\rho(y) = \begin{cases} \rho_1 - \rho_m e^{(y-0.25)/\Delta} & \text{for } 0.00 \leq y < 0.25 \\ \rho_2 + \rho_m e^{(0.25-y)/\Delta} & \text{for } 0.25 \leq y < 0.50 \\ \rho_2 + \rho_m e^{(y-0.75)/\Delta} & \text{for } 0.50 \leq y < 0.75 \\ \rho_1 - \rho_m e^{(0.75-y)/\Delta} & \text{for } 0.75 \leq y < 1.00, \end{cases} \quad (74)$$

where $\rho_1 = 1$, $\rho_2 = 2$, $\rho_m = (\rho_1 - \rho_2)/2$ and $\Delta = 0.025$. The velocity is set up as

$$v_x(y) = \begin{cases} v_1 - v_m e^{(y-0.25)/\Delta} & \text{for } 0.00 \leq y < 0.25 \\ v_2 + v_m e^{(0.25-y)/\Delta} & \text{for } 0.25 \leq y < 0.50 \\ v_2 + v_m e^{(y-0.75)/\Delta} & \text{for } 0.50 \leq y < 0.75 \\ v_1 - v_m e^{(0.75-y)/\Delta} & \text{for } 0.75 \leq y < 1.00 \end{cases} \quad (75)$$

with $v_1 = 0.5$, $v_2 = -0.5$, $v_m = (v_1 - v_2)/2$ and a small velocity perturbation in y -direction is introduced as $v_y = 0.01 \sin(2\pi x/\lambda)$ with the perturbation wave length $\lambda = 0.5$. In the linear regime, a Kelvin-Helmholtz instability grows in the incompressible limit on a characteristic time scale of

$$\tau_{\text{KH}} = \frac{(\rho_1 + \rho_2)\lambda}{\sqrt{\rho_1 \rho_2 |v_1 - v_2|}}, \quad (76)$$

with $\tau_{\text{KH}} \approx 1.06$ for the chosen parameters. For our tests, we chose again a polytropic equation of state with exponent $\Gamma = 5/3$.

We show in Fig. 5 a 512^2 realization of this test for all SPH versions. As in McNally et al. (2012), the traditional SPH version does not show any sign of growth until the end of the simulation ($t = 10$). All other versions show a healthy growth of the instability. V_4 is slightly lagging behind in the growth and shows an enormous degree of symmetry. Its Kelvin-Helmholtz billows also do not break

up into smaller scale substructures. As an additional experiment, we ran a low resolution version (64^2) of this test, see Fig. 6, which confirms this picture: V_0 does not grow at all, the Riemann solver version V_4 is seriously delayed, the standard gradient version (V_1) and the aLE-gradient version (V_2) grow healthily, but slightly slower than the RPK versions V_3 and V_5 .

To quantify these results further, we measure the growth rates (calculated exactly as in McNally et al. (2012)) for all versions at 64^2 , 128^2 , 256^2 and 512^2 , see Fig. 7. These results are compared with a high resolution (4096^2) simulation with the PENCIL code (Brandenburg & Dobler 2002). This plot confirms the visual impression that the Riemann solver version V_4 grows substantially slower than even the standard SPH kernel gradient version V_1 .

3.6 Rayleigh-Taylor test

In a Rayleigh-Taylor instability test, a density layer ρ_t rests on top of a layer with density $\rho_b < \rho_t$ in a constant acceleration field, e.g. due to gravity. When sinking down, the heavier fluid develops a characteristic "mushroom-like" pattern. Simulations with traditional SPH implementations have shown only retarded growth or even complete suppression of the instability (Abel 2011; Saitoh & Makino 2013). We adopt again a quasi-2D setup, but evolve the fluid with a full 3D code. For simplicity, we place 400 particles on a cubic lattice in the xy -domain $[-0.25, 0.25] \times [0, 1]$ and use 20 layers of particles in the z -direction, and also place 20 layers of particles as boundaries around this core region. The properties of the particles below $y = 0$ are "frozen" at the values of the initial conditions, and we multiply the temporal derivatives of particles with $y_a > 1$ with a damping factor

$$\xi = \exp \left\{ - \left(\frac{y_a - 1}{0.05} \right)^2 \right\}, \quad (77)$$

so that any evolution in this upper region is strongly suppressed. We apply periodic boundaries in the x -direction at $x = \pm 0.25$. Similar to Frontiere et al. (2017) we use $\rho_t = 2$, $\rho_b = 1$, a constant acceleration $\vec{g} = -0.5\hat{e}_y$ and

$$\rho(y) = \rho_b + \frac{\rho_t - \rho_b}{1 + \exp[-(y - y_t)/\Delta]} \quad (78)$$

with transition width $\Delta = 0.025$ and transition coordinate $y_t = 0.5$. We apply a small velocity perturbation to the interface

$$v_y(x, y) = \delta v_{y,0} [1 + \cos(8\pi x)][1 + \cos(5\pi(y - y_t))] \quad (79)$$

for y in $[0.3, 0.7]$ with an initial amplitude $\delta v_{y,0} = 0.025$, and we use a polytropic equation of state with exponent $\Gamma = 1.4$. The equilibrium pressure profile is given by

$$P(y) = P_0 - g\rho(y)[y - y_t] \quad (80)$$

with $P_0 = \rho_t/\Gamma$, so that the sound speed is near unity in the transition region.

The situation here is similar to the Kelvin-Helmholtz test: V_0 does hardly grow at all, the Riemann solver version V_4 grows slower than the other good gradient versions and, again, maintains a very high degree of symmetry. The other versions develop filigrane fine structures as they sink down. Once more, V_3 and V_5 show very similar performance, but are closely followed by the aLE-gradient version V_2 .

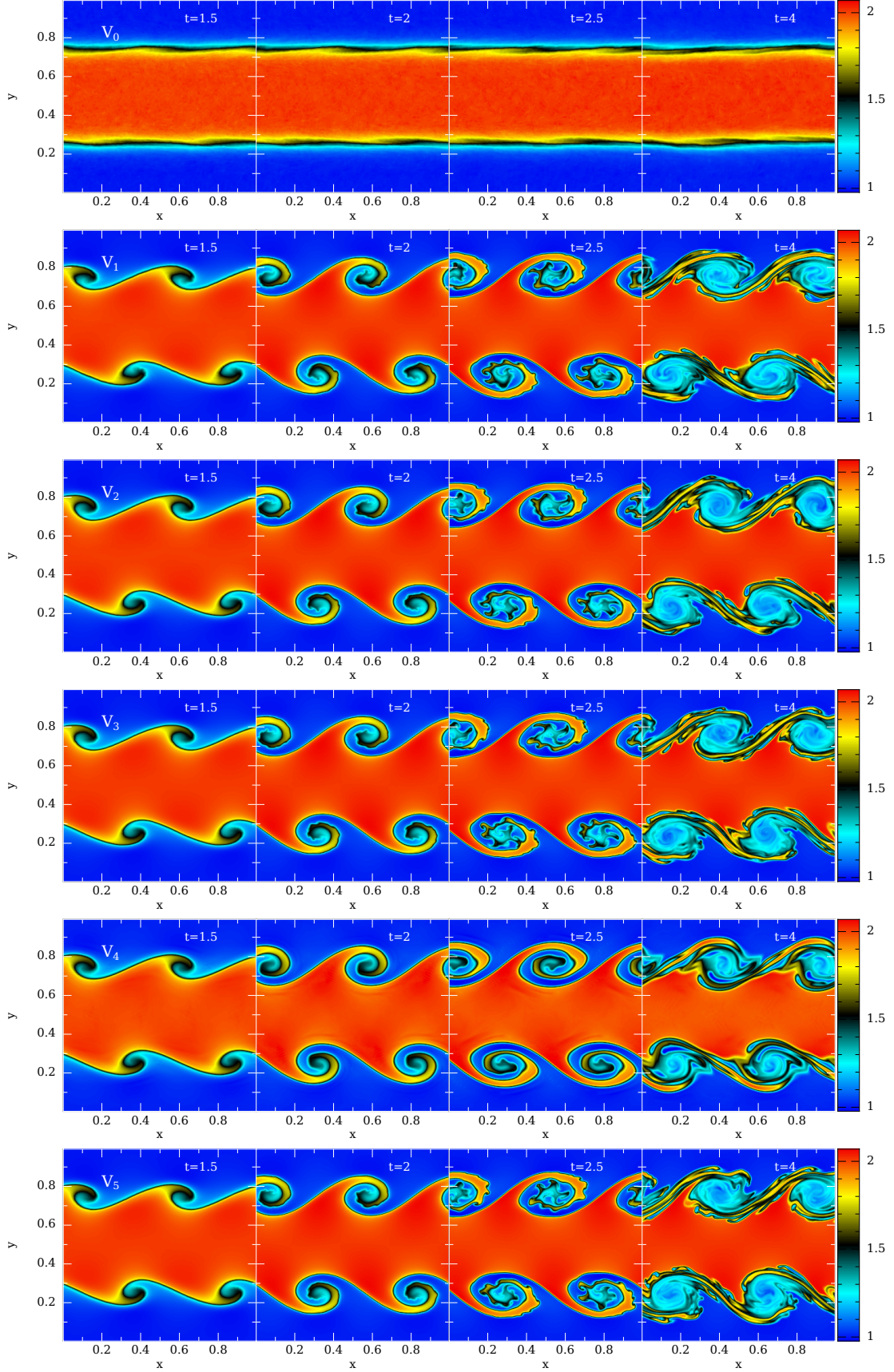


Figure 5. Kelvin-Helmholtz instability for all SPH versions at 512^2 .

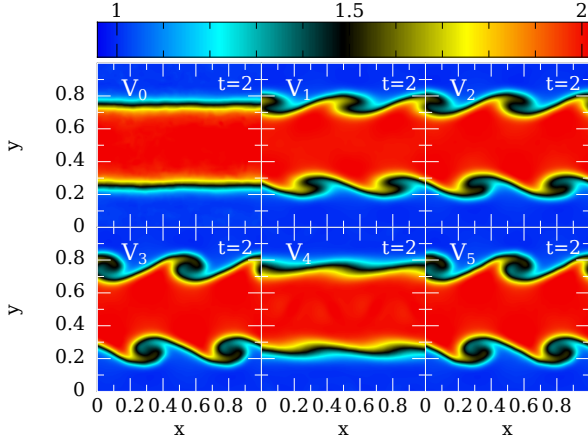


Figure 6. Density of Kelvin-Helmholtz instability at low resolution (64^2) for all versions.

3.7 Schulz-Rinne tests

Schulz-Rinne tests (Schulz-Rinne 1993) are very challenging 2D benchmarks (Schulz-Rinne 1993; Lax & Liu 1998; Kurganov & Tadmor 2002; Liska & Wendroff 2003). They are constructed so that four constant states meet at one corner, and the initial values are chosen so that an elementary wave, either a shock, a rarefaction, or a contact discontinuity, appears at each interface. During subsequent evolution, complex wave patterns emerge for which exact solutions are not known. Such tests have not often been shown for SPH. We are only aware of the work of Puri & Ramachandran (2014), applying Godunov SPH with approximate Riemann solvers, the tests in the MAGMA2 code (Rosswog 2020) and in a Riemann solver approach with reproducing kernels (Rosswog 2025). Here, we show three such tests. We place particles on a cubic lattice in a 3D slice thick enough so that the mid-plane is unaffected by edge effects (we use 20 particle layers in z -direction), so that 300×300 particles are within $[x_c - 0.3, x_c + 0.3] \times [y_c - 0.3, y_c + 0.3]$, where (x_c, y_c) is the contact point of the quadrants, and we use a polytropic exponent $\Gamma = 1.4$ in all tests. We refer to these Schulz-Rinne type problems as SR1-SR3³ and give their initial parameters for each quadrant in Table 1.

For the first test, see Fig. 9, V_3 and V_5 perform best, but closely followed by V_2 . They show a high degree of symmetry and "mushroom-like" structures in both forward and backward direction. The Riemann solver version V_4 seems to suppress at least the "backward mushroom" (at $x \approx 0.3$ and $y \approx 0.3$) and the "forward mushroom" (at $x \approx 0.25$ and $y \approx 0.25$) is not as crisp as for V_3 and V_5 . The gradient accuracy is important here for maintaining the symmetry, both standard kernel gradient versions (V_0 and V_1) show noticeable asymmetries.

The situation is very similar for the second test, see Fig. 10. Again V_0 hardly shows much structure, V_1 is already substantially better, V_4 is reluctant to curl in on the "rim of the mushroom", V_3 and V_5 are best, but closely followed by V_2 .

Practically the same can be said about the third Schulz-Rinne test, see Fig. 11. Once more, V_3 and V_5 perform best, but closely followed by V_2 , V_4 shows a delayed formation of the mushroom-like structure which is essentially suppressed in V_0 . It is also worth

³ In Kurganov & Tadmor (2002) these are tests have the numbers 3, 11, and 12.

Table 1. Initial conditions for the Schulz-Rinne-type 2D Riemann problems.

SR1; contact point: (0.3,0.3)				
variable	NW	NE	SW	SE
ρ	0.5323	1.5000	0.1380	0.5323
v_x	1.2060	0.0000	1.2060	0.0000
v_y	0.0000	0.0000	1.2060	1.2060
P	0.3000	1.5000	0.0290	0.3000
SR2; contact point: (0.0,0.0)				
variable	NW	NE	SW	SE
ρ	0.5313	1.0000	0.8000	0.5313
v_x	0.8276	0.1000	0.1000	0.1000
v_y	0.0000	0.0000	0.0000	0.7276
P	0.4000	1.0000	0.4000	0.4000
SR3; contact point: (0.0,0.0)				
variable	NW	NE	SW	SE
ρ	1.0000	0.5313	0.8000	1.0000
v_x	0.7276	0.0000	0.0000	0.0000
v_y	0.0000	0.0000	0.0000	0.7262
P	1.0000	0.4000	1.0000	1.0000

pointing out the spurious wave pattern that emerges in the case of V_2 , see e.g. the region $x > 0.3$ and $y > 0.1$.

4 SUMMARY

In this study we explored the impact of the gradient accuracy on the performance of various SPH formulations that are specified by the choice of a scalar Ψ , see Eqs. (42) to (45). Consistent with earlier studies, we found that $\Psi = \rho$ is an excellent choice and therefore we used this as a baseline model. Apart from the standard SPH kernel gradient we explored an approximation to the "linearly exact gradient" (aLE-gradients) and linearly reproducing kernel (RPK) gradients. The aLE-gradients become linearly exact in the limit of an exact partition of unity and they only cost the inversion of a small 3×3 matrix. The RPK kernels are constructed so that they exactly fulfill the discrete linear consistency relations, see Eq. (25), and their construction comes at a noticeable computational cost, for their explicit expressions see Appendix 2.2.2. Both aLE and RPK approaches massively improve the gradient accuracy, but while ensuring exact energy and momentum conservation, they sacrifice the exact conservation of angular momentum since the inter-particle forces can no longer be guaranteed to be exactly along the line connecting two particles.

In all but one SPH formulations we used shock dissipation, i.e. artificial viscosity and conductivity, and in the "jump terms" which are responsible for the dissipation, we use linearly reconstructed quantities limited by the van Albada slope limiter (van Albada et al. 1982). In addition to the slope-limited reconstruction, we steer the dissipation parameters, so that they decay to zero where they are not needed. The dissipation parameters are raised as indicated by a Cullen-Dehnen-type (CD) shock indicator reacting on $(\nabla \cdot \vec{v})/dt$, but we also add a sensitive trigger that measures local noise in the particle distribution. We compared these modern SPH formulations with a recent particle hydrodynamics approach (Rosswog

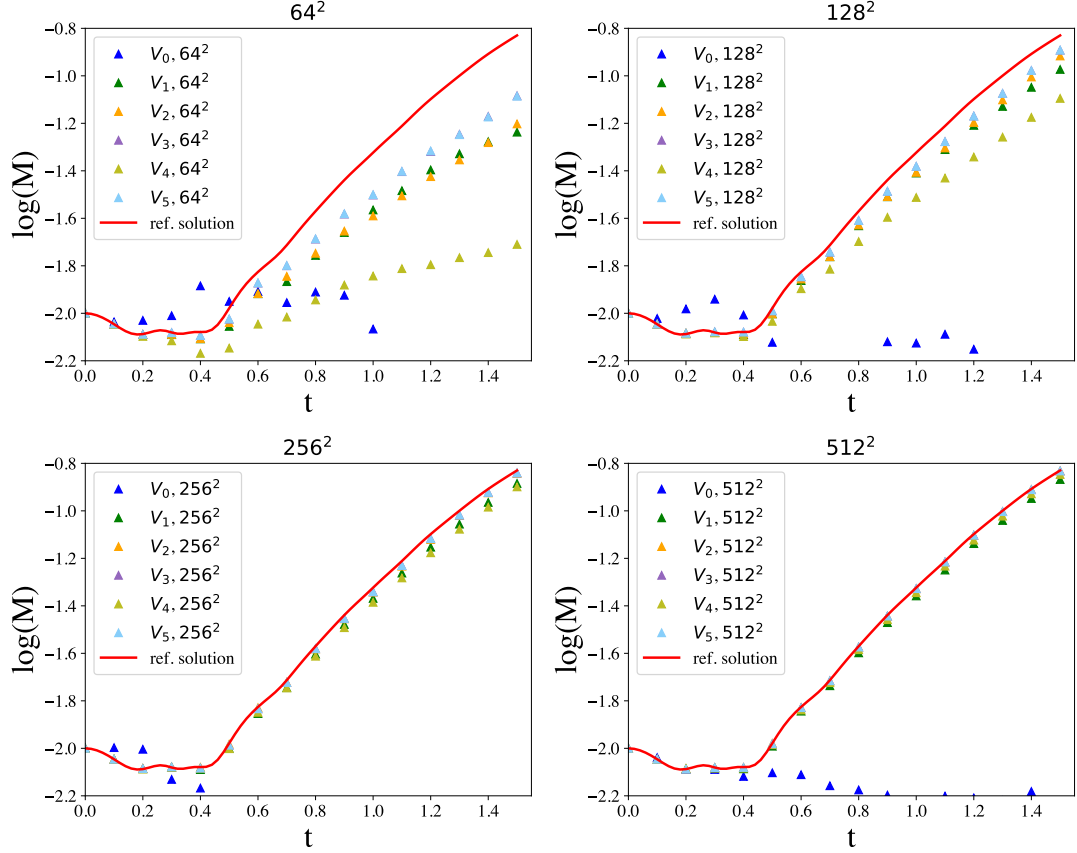


Figure 7. Mode growth at 64^2 , 128^2 , 256^2 and 512^2 compared to a very high resolution simulation (4096^2) obtained with the PENCIL code. Note that V_0 (dark blue triangles) never grows properly, not even at 512^2 and several of the V_0 symbols are below the shown scale. The versions V_3 and V_5 perform nearly identically and their symbols lie on top of each other so that only the symbols for V_5 are visible.

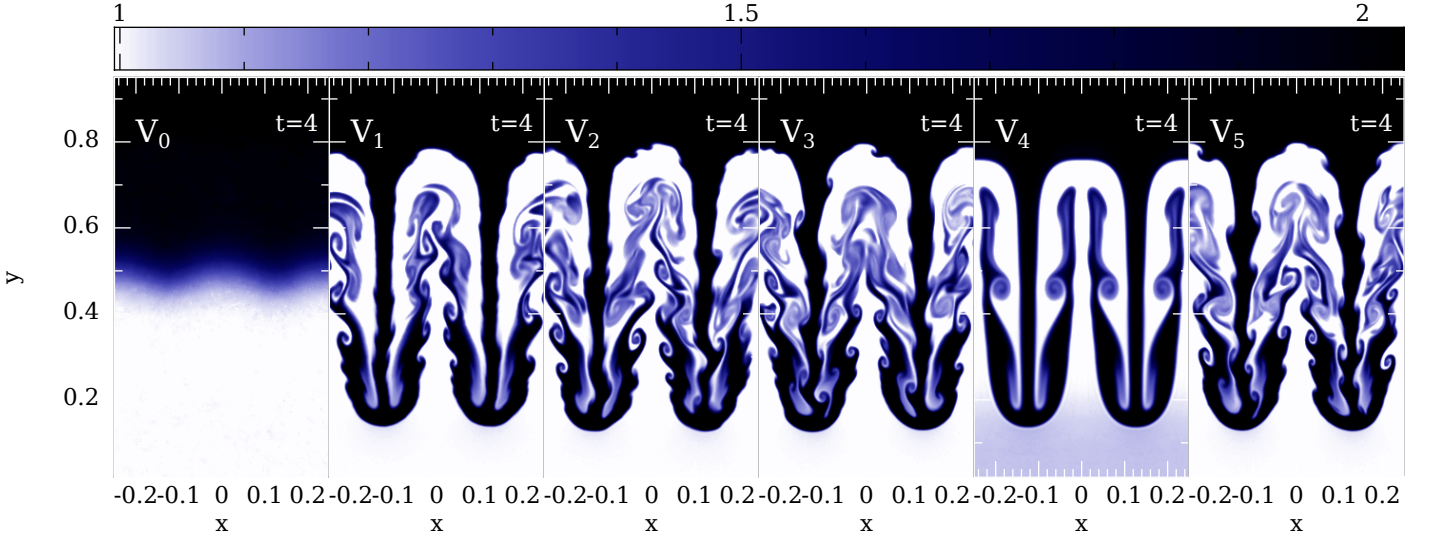


Figure 8. Density of Rayleigh-Taylor instability at 400^2 for all versions.

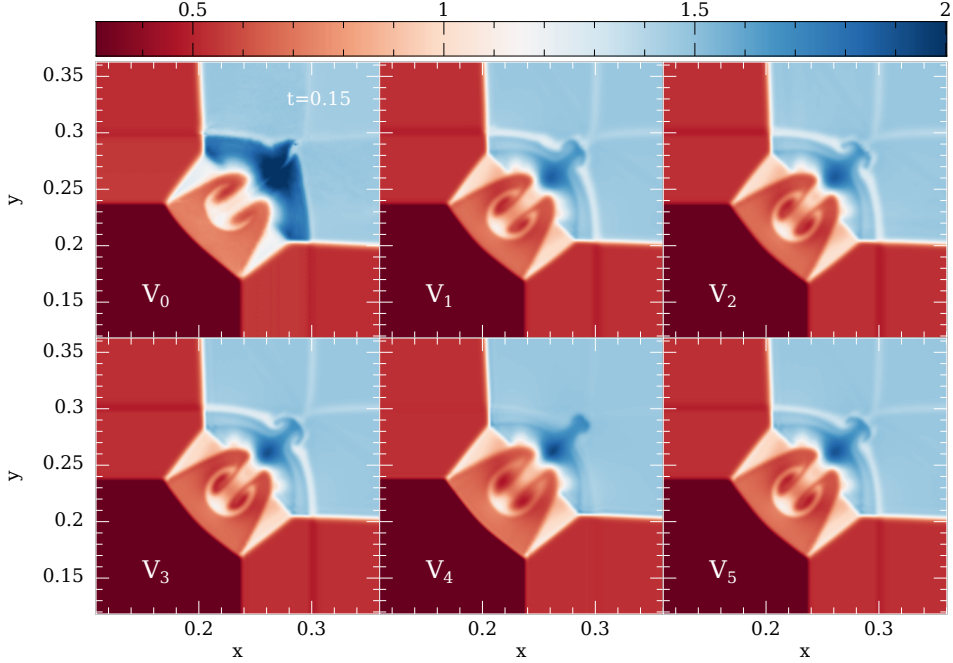


Figure 9. Schulz-Rinne test SR1 for all versions.

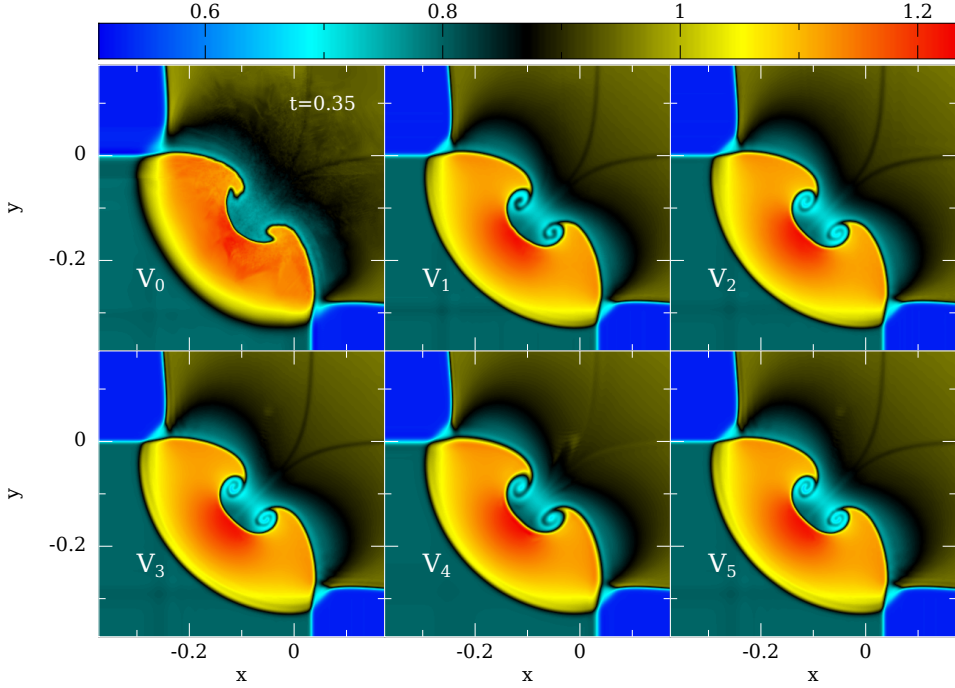


Figure 10. Schulz-Rinne test SR2 for all versions.

2025) that also uses RPKs, but applies Roe's Riemann solver instead of shock dissipation.

Our main results can be summarized as follows:

- Not too surprisingly, a major improvement compared to "old school" SPH (V_0) with constant dissipation and cubic spline kernels comes from the reduction of unwanted dissipation. The V_0 formula

gives reasonable results in shocks, but massively underperforms in all tests related to instabilities.

- Shock tests are not very sensitive to the gradient accuracy, only in Riemann problem 2, see Fig. 4, we find somewhat noisy inner regions for all but the RPK gradients. But we find that the gradient accuracy plays a major role for all tests that involve fluid instabilities, see Sec. 3.5, 3.6 and 3.7.

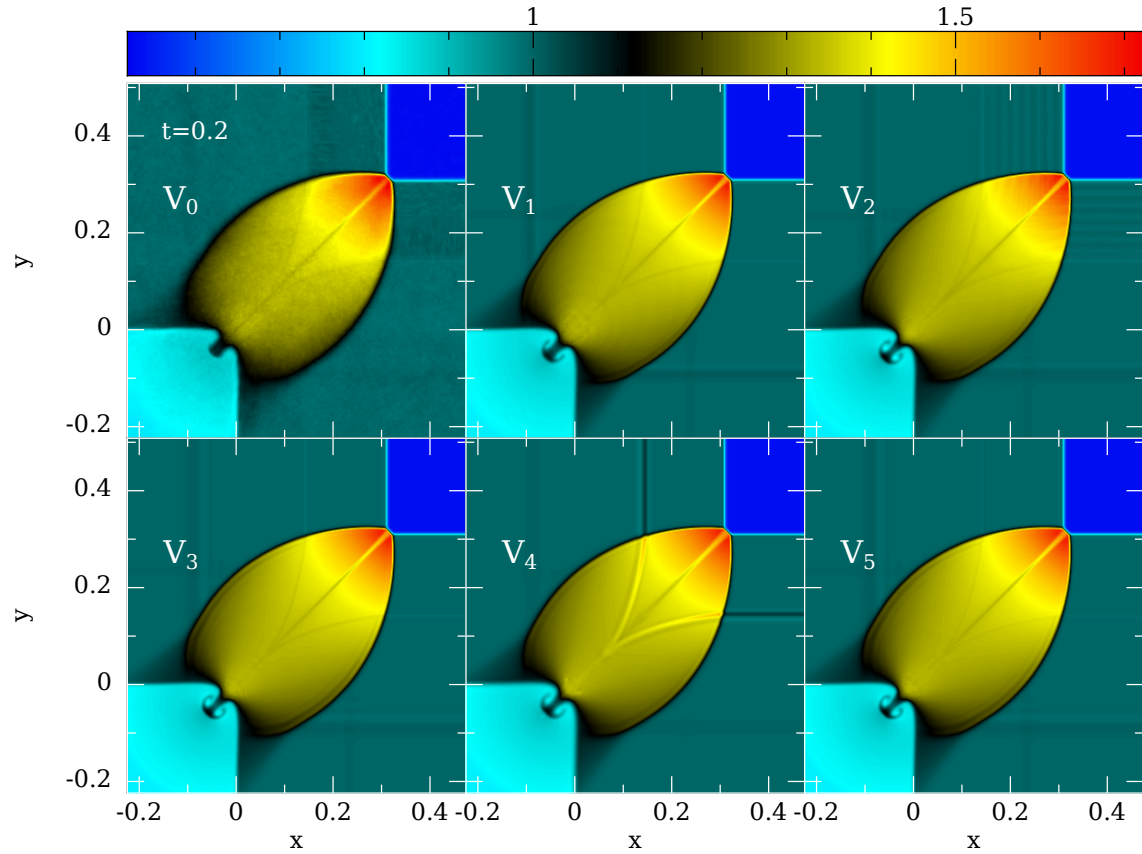


Figure 11. Schulz-Rinne test SR3 for all versions.

- As expected, the numerically most expensive gradients using reproducing kernels perform best, but they are closely followed by the substantially cheaper aLE gradients. The differences between the two show up mostly in the instability and the Schulz-Rinne tests. We also find the RPK gradients consistently trigger lower dissipation values, see Fig. C2, indicating a more accurate particle motion on the length scales of the kernel support.

- While the CD-type trigger works very well in shocks, we find that it does not trigger sufficient dissipation in the complex Schulz-Rinne tests, see the left column in Fig. C1. But together with our noise trigger it provides an appropriate amount of dissipation, see the right column in Fig. C1, and without triggering too much dissipation in the rather gentle fluid instability tests. We find this combination of shock and noise triggers accurate and robust.

- Comparing the shock dissipation approaches with the Riemann solver case, we find interesting differences. While the Riemann solver approach (V_4 in Sec. 2.4) has some advantage in the shock tests, producing the smallest amount of oscillations (although closely followed by V_3 and V_5), it produces more dissipation in rarefaction regions than the shock dissipation approach. This is simply because the Riemann solver dissipation is applied independent of whether the local flow is converging or diverging while the shock dissipation is only applied for converging flows. More interestingly, the Riemann solver approach shows some resistance for fluid instabilities to develop. In the fluid instability tests it enforces nearly perfect symmetry, but the instabilities grow substantially slower than in the shock dissipation cases. In fact, at very low resolution

(64^2), only the "old school" approach V_0 behaves worse than the Riemann solver approach V_4 , see Fig. 7.

The RPK approach is clearly a major improvement over standard SPH gradients. The aLE-gradients are less accurate, but we still find them very useful, mostly because of their simple implementation and negligible computational cost and in many of the shown tests they are nearly as good as the RPK approach. Based on this test suite, we consider our SPH version V_3 as the best one, but very closely followed by V_5 . The simpler V_2 version is still a substantial improvement over the standard SPH gradients. The standard kernel gradient SPH approach with good choices, V_1 , performs overall still pretty well. Due to its reluctance to let instabilities grow, we rank the Riemann solver version V_4 lower than the previous versions, despite its very good performance in shocks. While the best of these versions represent the current state-of-the-art for SPH-type hydrodynamics, further improvements of particle hydrodynamics is probably possible and should be explored in future work.

ACKNOWLEDGEMENTS

SR has been supported by the Swedish Research Council (VR) under grant number 2020-05044, by the research environment grant "Gravitational Radiation and Electromagnetic Astrophysical Transients" (GREAT) funded by the Swedish Research Council (VR) under Dnr 2016-06012, by the Knut and Alice Wallenberg Foundation under grant Dnr. KAW 2019.0112, by the Deutsche

Forschungsgemeinschaft (DFG, German Research Foundation) under Germany's Excellence Strategy - EXC 2121 "Quantum Universe" - 390833306 and by the European Research Council (ERC) Advanced Grant INSPIRATION under the European Union's Horizon 2020 research and innovation programme (Grant agreement No. 101053985).

The simulations for this paper have been performed on the facilities of North-German Supercomputing Alliance (HLRN), and at the SUNRISE HPC facility supported by the Technical Division at the Department of Physics, Stockholm University, and on the HUM-MEL2 cluster funded by the Deutsche Forschungsgemeinschaft (498394658). Special thanks go to Mikica Kocic (SU), Thomas Orjis and Hinnerk Stueben (both UHH) for their excellent support. Some plots have been produced with the software `splash` (Price 2007).

APPENDIX A: EXPLICIT EXPRESSIONS FOR REPRODUCING KERNELS

The gradient of the kernel \mathcal{W} with respect to position \vec{r}_a , $\partial_k \mathcal{W}_{ab} \equiv (\nabla_a)^k \mathcal{W}_{ab}$, reads

$$\begin{aligned} \partial_k \mathcal{W}_{ab} = & A_a B_a^k \bar{W}_{ab} + A_a \left(1 + B_a^i (\vec{r}_{ab})^i \right) \nabla_a^k \bar{W}_{ab} + \\ & \left(1 + B_a^i (\vec{r}_{ab})^i \right) \bar{W}_{ab} (\nabla_a^k A)_a + A_a (\vec{r}_{ab})^i (\nabla_a^k B)_a^i \bar{W}_{ab}. \end{aligned} \quad (\text{A1})$$

Taking the gradient of \mathcal{W}_{ba} with respect to \vec{r}_b , $\partial_k \mathcal{W}_{ba} \equiv (\nabla_b)^k \mathcal{W}_{ba}$, results in

$$\begin{aligned} \partial_k \mathcal{W}_{ba} = & A_b B_b^k \bar{W}_{ab} - A_b \left(1 - B_b^i (\vec{r}_{ab})^i \right) \nabla_b^k \bar{W}_{ab} + \\ & \left(1 - B_b^i (\vec{r}_{ab})^i \right) \bar{W}_{ab} (\nabla_b^k A)_b - A_b (\vec{r}_{ab})^i (\nabla_b^k B)_b^i \bar{W}_{ab}, \end{aligned} \quad (\text{A2})$$

where we have used $\bar{W}_{ab} = \bar{W}_{ba}$, $\vec{r}_{ba} = -\vec{r}_{ab}$ and $\nabla_b^k \bar{W}_{ba} = -\nabla_a^k \bar{W}_{ab}$. The derivations that lead to the explicit expressions for A_a , B_a and their derivatives are straight-forward, but lengthy. One needs the discrete moments at position a

$$(M_0)_a \equiv \sum_b V_b \bar{W}_{ab} \quad (\text{A3})$$

$$(M_1^i)_a \equiv \sum_b (\vec{r}_{ab})^i V_b \bar{W}_{ab} \quad (\text{A4})$$

$$(M_2^{ij})_a \equiv \sum_b (\vec{r}_{ab})^i (\vec{r}_{ab})^j V_b \bar{W}_{ab} \quad (\text{A5})$$

and their derivatives

$$(\partial_k M_0)_a = \sum_b V_b \nabla_a^k \bar{W}_{ab} \quad (\text{A6})$$

$$(\partial_k M_1^i)_a = \sum_b V_b \left[(\vec{r}_{ab})^i (\nabla_a^k \bar{W}_{ab}) + \delta^{ki} \bar{W}_{ab} \right] \quad (\text{A7})$$

$$(\partial_k M_2^{ij})_a = \sum_b V_b \left[(\vec{r}_{ab})^i (\vec{r}_{ab})^j (\nabla_a^k \bar{W}_{ab}) + (\vec{r}_{ab})^i \delta^{jk} \bar{W}_{ab} + (\vec{r}_{ab})^j \delta^{ik} \bar{W}_{ab} \right] \quad (\text{A8})$$

With these expressions at hand, one can straight forwardly calculate the kernel parameters

$$A_a = \frac{1}{(M_0)_a - (M_2^{ij})_a^{-1} (M_1^i)_a (M_1^j)_a} \quad (\text{A9})$$

$$B_a^i = -(M_2^{ij})_a^{-1} (M_1^j)_a \quad (\text{A10})$$

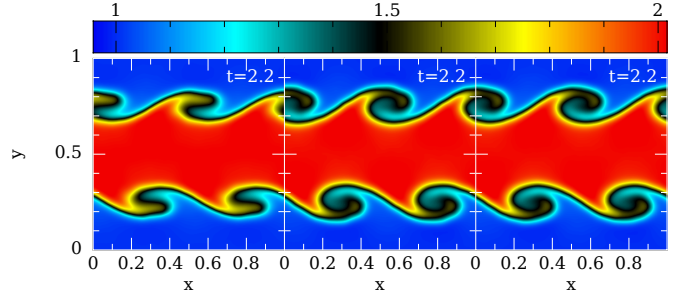


Figure B1. Comparison of a low resolution (64^2) Kelvin-Helmholtz test for different choices of the free scalar Ψ . The left panel shows the results for "vanilla ice SPH" ($\Psi = 1$), the middle for the Hernquist and Katz symmetrization ($\Psi = \rho/\sqrt{P}$), and the right panel uses our default choice ($\Psi = \rho$). Clearly, the "vanilla ice" version grows slower than the other two.

and their somewhat lengthy, but otherwise straight forwardly calculable, derivatives which are needed for $\partial_k \mathcal{W}_{ab}$, see Eq. (A1)

$$\begin{aligned} \partial_k A_a = & -A_a^2 \left[(\partial_k M_0)_a - 2(M_2^{ij})_a^{-1} (M_1^j)_a (\partial_k M_1^i)_a \right. \\ & \left. + (M_2^{il})_a^{-1} (\partial_k M_2^{lm})_a (M_2^{mj})_a^{-1} (M_1^j)_a (M_1^l)_a^i \right] \end{aligned} \quad (\text{A11})$$

and

$$\partial_k B_a^i = -(M_2^{ij})_a^{-1} (\partial_k M_1^j)_a + (M_2^{il})_a^{-1} (\partial_k M_2^{lm})_a (M_2^{mj})_a^{-1} (M_1^j)_a. \quad (\text{A12})$$

APPENDIX B: COMPARISON FOR DIFFERENT COMMON CHOICES OF Ψ

We had given in Sec. 2.4 SPH formulations that contain a scalar field Ψ and we want to show here a concise comparison between three common choices. Each time we use the same density summation, Eq. (47), and we use the gradients $(\nabla \mathcal{W})_{ab}$, see Eq. (28). For $\Psi = 1$ one recovers (apart from using the RPK gradients) the "vanilla ice" symmetrization of SPH that was also used in version V_0 . For $\Psi = \rho/\sqrt{P}$ one recovers the Hernquist & Katz (1989) symmetrization

$$\frac{d\vec{v}_a}{dt} = -\sum_b m_b \left(2 \frac{\sqrt{P_a P_b}}{\rho_a \rho_b} \right) (\nabla \mathcal{W})_{ab} \quad (\text{B1})$$

$$\frac{du_a}{dt} = \sum_b m_b \left(\frac{\sqrt{P_a P_b}}{\rho_a \rho_b} \right) \vec{v}_{ab} \cdot (\nabla \mathcal{W})_{ab}, \quad (\text{B2})$$

and for $\Psi = \rho$ one finds our default symmetrization that is used in the SPH formulations V_1 , V_2 and V_3 .

Here we use each time exactly the same shock dissipation, see Sec. 2.3, kernel, initial data and gradients, the only change is the *symmetry* in the equations. We illustrate the differences with one instability, the Kelvin-Helmholtz instability, and a shock with strong density gradients, a Sedov explosion test. For both tests we have reference solutions to compare with and both tests are set up exactly as described in the main text.

We perform the Kelvin-Helmholtz test at a resolution of only 64^2 so that potential differences should be clearly visible. For the Kelvin-Helmholtz test the vanilla ice symmetrization ($\Psi = 1$) clearly grows slower than the other two which perform here similarly, see Fig. B1. On close inspection one finds that the $\Psi = \rho$ symmetrization grows fastest, which is also visible in the measured growth rates, see Fig. B2.

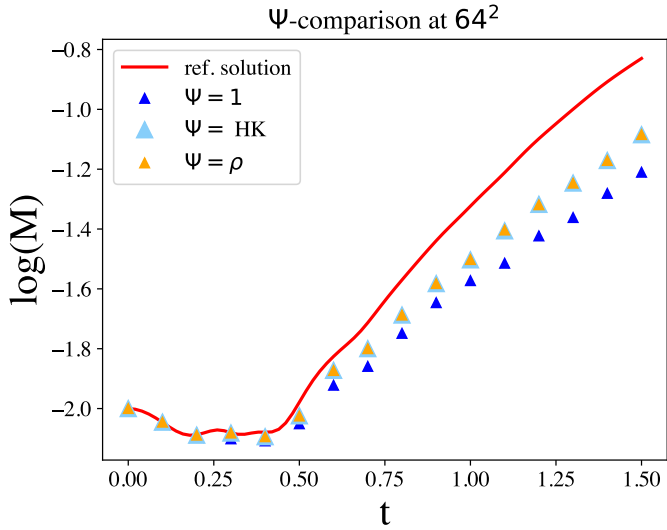


Figure B2. Comparison of a low resolution (64^2) Kelvin-Helmholtz test for the different choices of the free scalar Ψ that are shown in Fig. B1. Note that the symbol for the Hernquist and Katz symmetrization ("HK") has been increased since otherwise it would not be visible below the $\Psi = \rho$ results.

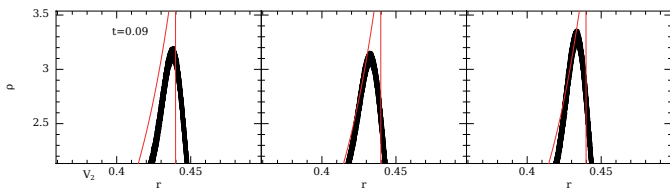


Figure B3. Comparison of the peak heights reached in the Sedov explosion test (128^2 ; all particles plotted) for different choices of the free scalar: $\Psi = 1$ (left panel, "vanilla ice"), $\Psi = \rho/\sqrt{P}$ (middle, Hernquist-Katz) and $\Psi = \rho$ (right panel; our default choice). Here $\Psi = \rho$ clearly reaches the largest peak height.

In Fig. B3 we zoom in on the density peak of a 128^2 Sedov test for all three versions. Also here, the $\Psi = \rho$ performs best, now having a clear advantage over the Hernquist-Katz symmetrization. In summary, from the explored choices $\Psi = \rho$ has a clear advantage over the other possibilities. We are not aware of any disadvantage of this formulation and therefore use it as our default.

APPENDIX C: EFFECTIVENESS OF THE NOISE TRIGGER FOR DISSIPATION

We want to briefly illustrate the impact of the noise trigger, see Eq. (39). The functional form of this trigger was suggested by Rosswog (2015a), though in a special-relativistic context. Contrary to the original suggestion, we choose here a rather small prefactor ($=0.01$) in the reference value, see Eq. (40). This reference value decides on how to translate the trigger T_a^n into a dissipation parameter value, $\alpha_{a,\text{noise}}$.

To illustrate that such an additional triggering on noise is really desirable and that the suggested trigger is really effective, we run a lower-resolution simulation (200^2) of the Schulz-Rinne test 3 with SPH version V_3 , once using only the Cullen & Dehnen (2010) (CD) trigger as described in Sec. 2.3 and once using in addition our noise trigger, see Fig. C1. In the CD-only case not sufficient dissipation is

triggered and a number of spurious wiggles appear (right column) which are efficiently suppressed by the suggested noise trigger (left column).

Note that while the Wendland C4 kernel is the best overall compromise, in this test a high order WH_8 kernel Cabezon et al. (2008) does not even show the small post-shock wiggle that is still visible in the upper left panel.

REFERENCES

Abel T., 2011, MNRAS, 413, 271
 Agertz O., Moore B., Stadel J., Potter D., Miniati F., Read J., Mayer L., Gawryszczak A., Kravtsov A., Nordlund Å., Pearce F., Quilis V., Rudd D., Springel V., Stone J., Tasker E., Teyssier R., Wadsley J., Walder R., 2007, MNRAS, 380, 963
 Bambi C., Mizuno Y., Shashank S., Yuan F., eds, 2025, 'SPHINCS_BSSN: Numerical Relativity with Particles' in book 'New Frontiers in GRMHD Simulations'. Springer Series in Astrophysics and Cosmology, Springer Nature Singapore
 Benz W., 1990, in Buchler J. R., ed., Numerical Modelling of Nonlinear Stellar Pulsations Problems and Prospects Smooth Particle Hydrodynamics - a Review. p. 269
 Brandenburg A., Dobler W., 2002, Computer Physics Communications, 147, 471
 Cabezon R. M., Garcia-Senz D., Escartin J. A., 2012, A & A, 545, A112
 Cabezon R. M., Garcia-Senz D., Relano A., 2008, Journal of Computational Physics, 227, 8523
 Christensen R. B., 1990, Nuclear Explosives Code Developers Conference, volume UCRL-JC-105269. Lawrence Livermore National Lab, Lawrence Livermore Technical Report., UCRL-JC-105269
 Cullen L., Dehnen W., 2010, MNRAS, 408, 669
 Diener P., Rosswog S., Torsello F., 2022, European Physical Journal A, 58, 74
 Du Q., Faber V., Gunzburger M., 1999, SIAM Review, 41, 637
 Frontiere N., Raskin C. D., Owen J. M., 2017, Journal of Computational Physics, 332, 160
 Gafton E., Rosswog S., 2011, MNRAS, 418, 770
 Garcia-Senz D., Cabezon R., Escartin J., 2012, A & A, 538, A9
 Gingold R. A., Monaghan J. J., 1977, MNRAS, 181, 375
 Hernquist L., Katz N., 1989, ApJS, 70, 419
 Kitajima K., Inutsuka S.-i., Seno I., 2026, Journal of Computational Physics, 545
 Kurganov A., Tadmor E., 2002
 Lax P., Liu X., 1998, SIAM J. Sci. Comput, 19, 319
 Liptai D., Price D. J., 2019, MNRAS, 485, 819
 Liska R., Wendroff B., 2003, SIAM J. Sci. Comput., 25, 995
 Liu G., Liu M., 2003, Smoothed Particle Hydrodynamics: A Meshfree Particle Method. World Scientific
 Liu W. K., Jun S., Zhang Y. F., 1995, International Journal for Numerical Methods in Fluids, 20, 1081
 Lucy L., 1977, The Astronomical Journal, 82, 1013
 Magnall S. J., Price D. J., Lasky P. D., Macpherson H. J., 2023, Phys. Rev. D, 108, 103534
 Mattsson A. E., Rider W. J., 2015, International Journal for Numerical Methods in Fluids, 77, 400
 McNally C. P., Lyra W., Passy J.-C., 2012, ApJS, 201, 18
 Monaghan J., Gingold R., 1983, J. Comp. Phys., 52, 374
 Monaghan J. J., 1992, Ann. Rev. Astron. Astrophys., 30, 543
 Monaghan J. J., 2005, Reports on Progress in Physics, 68, 1703

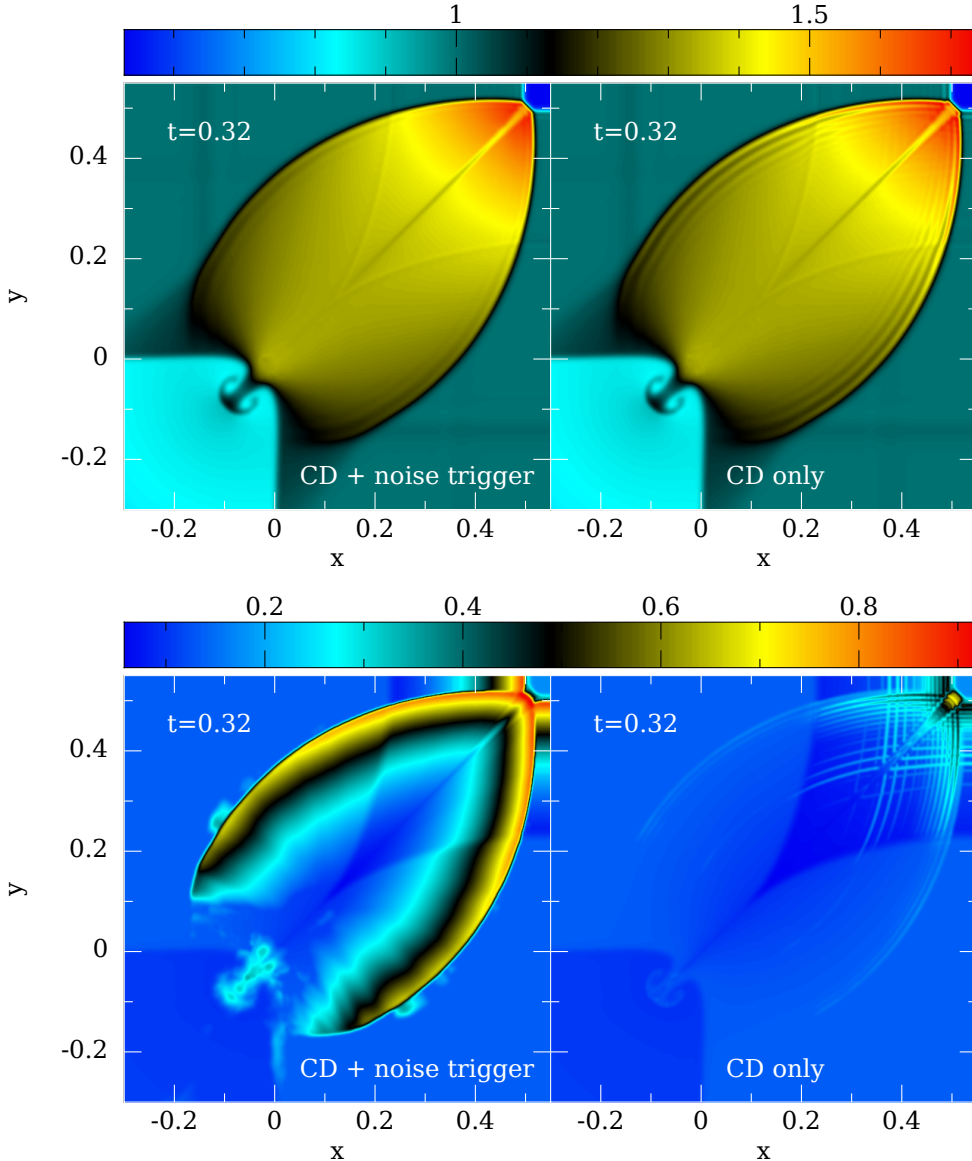


Figure C1. Comparison of a lower resolution (200^2) simulation of Schulz Rinne test 3, once using the Cullen-Dehnen-type (CD) trigger as described in the main text together with our noise trigger (left column) and once relying exclusively on the CD trigger. The upper row shows density, the lower one the dissipation parameter α . Clearly the use of noise trigger efficiently suppresses the spurious waves that are visible the “CD only” case.

Monaghan J. J., 2012, Annual Review of Fluid Mechanics, 44, 323
 Morris J., Monaghan J., 1997, J. Comp. Phys., 136, 41
 Oger G., Doring M., Alessandrini B., Ferrant P., 2007, Journal of Computational Physics, 225, 1472
 Parshikov A. N., Medin S. A., 2002, Journal of Computational Physics, 180, 358
 Price D., 2004, PhD thesis, University of Cambridge, arXiv:astro-ph/0507472
 Price D. J., 2007, Publications of the Astronomical Society of Australia, 24, 159
 Price D. J., 2008, Journal of Computational Physics, 227, 10040
 Price D. J., 2012, Journal of Computational Physics, 231, 759
 Puri K., Ramachandran P., 2014, Journal of Computational Physics, 270, 432

Quinlan N., Tong M., 2021, International Journal of Computational Fluid Dynamics, 35, 1
 Read J. I., Hayfield T., 2012, MNRAS, 422, 3037
 Read J. I., Hayfield T., Agertz O., 2010, MNRAS, p. 767
 Roe P. L., 1986, Annual Review of Fluid Mechanics, 18, 337
 Rosswog S., 2009, New Astronomy Reviews, 53, 78
 Rosswog S., 2010a, J. Comp. Phys., 229, 8591
 Rosswog S., 2010b, Classical and Quantum Gravity, 27, 114108
 Rosswog S., 2011, Springer Lecture Notes in Computational Science and Engineering, “Meshfree Methods for Partial Differential Equations V”, Eds. M. Griebel, M.A. Schweitzer, Heidelberg, p. 89-103
 Rosswog S., 2015a, MNRAS, 448, 3628
 Rosswog S., 2015b, Living Reviews of Computational Astrophysics (2015), 1

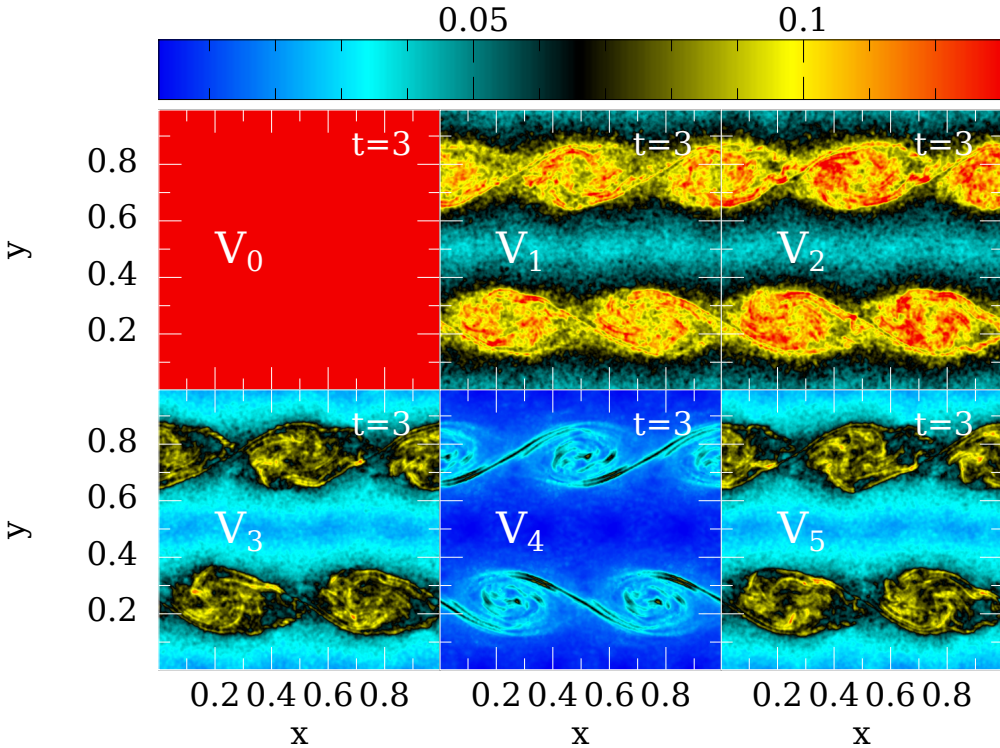


Figure C2. Values of the dissipation parameter α for the different versions in a Kelvin-Helmholtz test (512^2). For visibility reasons we cut the colour bar at a maximum of 0.13. Note that for V_4 the dissipation parameter is triggered exactly as in the other cases, but it is not used, since the dissipation comes from the Riemann solver. The α -value however can still indicate the noise on the kernel level. Note that the RPK gradients (V_3, V_4, V_5) trigger noticeably less dissipation than either kernel gradient (V_1) or the aLE gradients (V_2).

Rosswog S., 2020, MNRAS, 498, 4230
 Rosswog S., 2025, CMES - Computer Modeling in Engineering and Sciences, 143, 1713
 Rosswog S., 2026, Living Reviews of Computational Astrophysics, submitted
 Rosswog S., Diener P., 2021, Classical and Quantum Gravity, 38, 115002
 Rosswog S., Price D., 2007, MNRAS, 379, 915
 Rosswog S., Torsello F., Diener P., 2023, Front. Appl. Math. Stat., 9
 Saitoh T. R., Makino J., 2013, ApJ, 768, 44
 Sandnes T. D., Eke V. R., Kegerreis J. A., Massey R. J., Ruiz-Bonilla S., Schaller M., Teodoro L. F. A., 2025, Journal of Computational Physics, 532, 113907
 Schulz-Rinne C. W., 1993, SIAM Journal of Mathematical Analysis, 24, 76
 Sedov L. I., 1959, Similarity and Dimensional Methods in Mechanics
 Taylor G., 1950, Proceedings of the Royal Society of London Series A, 201, 159
 Tejeda E., Gafton E., Rosswog S., Miller J. C., 2017, MNRAS, 469, 4483
 Toro E., Riemann solvers and numerical methods for fluid dynamics, Springer 2009
 Valdarnini R., 2012, A & A, 546, A45
 van Albada G. D., van Leer B., Roberts W. W. J., 1982, A & A, 108, 76
 Wadsley J. W., Keller B. W., Quinn T. R., 2017, MNRAS, 471,

2357
 Wendland H., 1995, Advances in Computational Mathematics, 4, 389